# Batholith tectonics: Formation and deformation of ghost stratigraphy during assembly of the mid-crustal Andalshatten batholith, central Norway

**Heather S. Anderson[1,*], Aaron S. Yoshinobu[1,†], Øystein Nordgulen[2], and Kevin Chamberlain[3]**
[1]*Department of Geosciences, Texas Tech University, Lubbock, Texas 79409-1053, USA*
[2]*Norwegian Geological Survey, Leiv Eirikssons 39, 7491 Trondheim, Norway*
[3]*Department of Geology and Geophysics, University of Wyoming, Laramie, Wyoming 82071, USA*

## ABSTRACT

**The Andalshatten batholith (322 km², >700 km³) is a predominantly granodioritic high-K, calc-alkaline igneous body that was assembled in the mid-crust across four lithologically distinct nappes within the Helgeland Nappe Complex, central Norway. Extensive vertical and horizontal exposures of metamorphic screens and xenoliths within the batholith provide an unparalleled view of the nature of magma emplacement, host rock displacement, and batholith assembly, i.e., batholith tectonics. The mapped intrusion consists of at least five distinct lithologic phases, including schlieren-banded to gneissic granodiorite (11% of batholith area), coarse-crystalline to K-feldspar megacrystic granodiorite (69%), amphibole-bearing diorite (11%), tonalite (2%), and minor leucogranite. Contacts between phases are both sharp and/or gradational and are interpreted to reflect comagmatic behavior over the duration of crystallization of the phases separated by a given contact. New chemical abrasion–thermal ionization mass spectrometry $^{206}Pb/^{238}U$ zircon weighted mean ages of 442.67 ± 0.14 Ma and 441.53 ± 0.40 Ma for 2 samples of the voluminous megacrystic granodiorite from disparate localities indicate distinct periods of zircon crystallization separated by ~1 Ma; titanite ages for these samples are 441.30 ± 0.21 Ma and 436.10 ± 2.80 Ma, respectively. No observable contacts were identified between these two lithologically similar localities.**

**Of the mapped intrusion area, ~8% (>24 km²) comprises screens (kilometer scale) and xenoliths (subkilometer scale) of metamorphic rocks that reflect the skeletal framework of the host rock nappes into which the granodioritic magmas intruded. This ghost stratigraphy maintains broad continuity with host rock lithology and structural trends. The largest screens show no evidence of internal, emplacement-related ductile deformation, but appear to be rigidly rotated into subparallelism with the western host rock contact, presumably during subsequent magma injection into the batholith. In contrast, xenoliths underwent rotation, translation, and internal deformation in the magma. The scale dependence of synmagmatic deformation of screens and xenoliths is likely the result of smaller blocks becoming thermally equilibrated with the surrounding magma and thus deforming by ductile mechanisms in a magma with increasing yield strength due to crystallization.**

**We interpret the Andalshatten batholith to have been assembled by at least five spatially distinct, elongate batches of magma over a minimum duration 600 ka to 1.7 Ma, including significant recharge events involving dioritic magmas. Local space for batholith assembly was accommodated by brittle and ductile deformation, including viscous flow of host rocks in a dynamothermal contact aureole. Viscous flow was facilitated by reactivation of existing structures (e.g., tightening of interlimb fold angles), recrystallization, and penetrative foliation development, resulting in near-field lateral and downward-directed displacement of host rocks along the western margin during batholith expansion and growth. Emplacement of dioritic magmas added heat and mass to the growing reservoir, enabling significant magnitudes of internal, hypersolidus flow, magmatic foliation development, mechanical mingling, and screen deformation. These observations and data sets are consistent with the hypothesis of multiple recharge events in a magma chamber that was partially molten over reasonably large spatial scales, thereby allowing screens and xenoliths to be incorporated and displaced and/or deformed.**

## INTRODUCTION

Batholiths and their enclosing host rocks provide a composite view of the time- and space-integrated physical and chemical processes that result in the focused collection of magma in the crust. However, the preserved record as exposed in exhumed paleoarcs is incomplete, leading to a variety of disparate and often conflicting models to account for how magmas are emplaced and batholiths are assembled. The study of large volume magmatic arc terranes *sensu lato* has produced a myriad of observations (Bateman, 1992; Ciavarella and Wyld, 2008), measurements (Ague and Brimhall, 1988; McCaffrey and Petford, 1997; de Saint Blanquat et al., 2006), geophysical images (Paulatto et al., 2012), and hypotheses (Tikoff and Teyssier, 1992; Tobisch et al., 1995; Petford, 1996; Bartley et al., 2008) that explain our current understanding of how magmas intrude the crust to form plutons and batholiths. Yet, a very contentious debate continues to thread the literature and professional conferences on magma emplacement studies (for a historical perspective, see Gilluly, 1948; Krauskopf, 1968; Glazner and Bartley, 2006, 2008; Clarke and Erdmann, 2008; Paterson et al., 2008; Yoshinobu and Barnes, 2008; Glazner et al., 2010).

Two related foci of study that have generated recent debate include (1) the mechanisms of magma emplacement and local space creation, i.e., the so-called plutonic "room problem," and (2) whether large batholiths were ever entirely

*Present address: ExxonMobil, 396 W. Greens Road, CORP-WGR-354, Houston, Texas 77067, USA
†Corresponding author.
§Emails: Anderson: heather.s.anderson@exxonmobil.com; Yoshinobu: aaron.yoshinobu@ttu.edu; Øystein: øystein.nordgulen@ngu.no; Chamberlain: kchamber@uwyo.edu.

*Geosphere*; June 2013; v. 9; no. 3; p. 667–690; doi:10.1130/GES00824.1; 17 figures; 1 table; 1 supplemental file.
Received 21 May 2012 ♦ Revision received 24 January 2013 ♦ Accepted 3 February 2013 ♦ Published online 17 April 2013

partially molten or, instead, assembled by incremental emplacement of numerous magma batches that cycled across their solidi depending on the rate of replenishment (e.g., Daly, 1903a, 1903b; Marsh, 1982; Hutton, 1996; Petford, 1996; Glazner et al., 2004; Cruden, 2006; Glazner and Bartley, 2006; Schoene et al., 2012).

Prompted by early geochronological studies (e.g., Stern et al., 1981; Chen and Moore, 1982) that inferred that batholiths may crystallize over millions of years, thermal models have demonstrated that a single mapped intrusion may record a protracted duration of crystallization and that portions of the growing pluton may be fully crystallized while other portions may be partially molten (Hardee, 1982; Hanson and Glazner, 1995; Yoshinobu et al., 1998; Nabelek et al., 2012). Recent high-precision U-Pb studies (e.g., Coleman et al., 2004; Matzel et al., 2006; Schaltegger et al., 2009; Schoene et al., 2012) have verified these simulations and demonstrate that mapped intrusion geometries may be the result of multiple events of magma emplacement, crystallization, and solidification, even where contacts between two units are gradational or not observed (e.g., Memeti et al., 2010). If a single mapped intrusion is constructed by multiple batches of solidifying magma over some duration, then it is probable that processes such as magma mixing, assimilation, fractional crystallization, and melt-rock reaction, as well as structural processes such as foliation development, may occur at a much finer spatial and temporal scale within the intrusion (i.e., over the time and length scales of individual batch emplacement). Furthermore, the mechanical evolution of the system may cycle through oscillating episodes of viscous and brittle deformation over the duration of batholith assembly (e.g., Huber et al., 2011). Therefore, it becomes critical to attempt to (1) evaluate the spatial dimensions of magma batches that feed a growing intrusion, (2) assess the relative contribution of deformation mechanisms that accompany magma emplacement into preexisting rocks and magmas (i.e., the space problem), and (3) assess the scale of geochemical and textural variation within a mapped intrusion that may be due to in situ versus in transit or source-related geological phenomena.

This study presents new field, structural, and geochronological data from the mid-crustal Andalshatten batholith, central Norwegian Caledonides, a relatively large volume of magma added to the middle crust ca. 442 Ma. The batholith intruded four nappes, each with distinctive lithologies, and pre-emplacement metamorphic and structural histories. It is important that the batholith preserves numerous screens and xenoliths ranging from the kilometer to millimeter scale in superbly exposed, glacially cut three-dimensional outcrops and vertical cliff faces. Such exposures provide an unprecedented range of scales of observation to study the processes attending batholith assembly. This research will evaluate the following: (1) the mechanisms of magma emplacement and possible durations of magma crystallization; (2) the processes by which xenoliths and screens are incorporated into the batholith; and (3) the spatial scales of potential magma batches and magmatic flow, and the implications for the size of the active or partially molten magma chambers in arc settings.

## GEOLOGIC SETTING OF THE ANDALSHATTEN BATHOLITH

### Host Rock Framework of the Andalshatten Batholith, Helgeland Nappe Complex

From west to east (structurally lowest to highest), the Andalshatten batholith intruded the Sauren-Torghatten, Lower, Middle, and Upper Nappes of the Helgeland Nappe Complex (Fig. 1; Thorsnes and Løseth, 1991; Nordgulen et al., 1993; Yoshinobu et al., 2002). The nappes are distinct in lithology, detrital zircon populations, metamorphic grade, and structural history (Kollung, 1967; Myrland, 1972; Gustavson, 1978; Barnes et al., 2007; Thorsnes and Løseth, 1991). The structurally lowest unit is the Sauren-Torghatten Nappe, which consists of lower to middle amphibolite-grade pelitic and psammitic schists, conglomerates, and calc-silicate rocks that unconformably overlie fragmented ultramafic bodies (Heldal, 1987, 2001; Heldal and Hjelmeland, 1988; Yoshinobu et al., 2002). The age of deposition of this unit is determined to be Ordovician based on a detrital zircon date of 481.7 ± 2.5 Ma from a metasandstone (Barnes et al., 2007) and crosscutting relationships with the Andalshatten batholith (see following Geochronology discussion). Rocks of the Lower Nappe consist of migmatite, quartzofeldspathic gneiss, calcareous schist, marble, and calc-silicate rocks. Metamorphic grade ranges from amphibolite to granulite facies. Pure calcite marbles with distinctive Sr and C isotopic signatures indicate deposition during Neoproterozoic time (Trønnes, 1994; Trønnes and Sundvoll, 1995; Sandøy, 2003; see Melezhik et al., 2005, for discussion of the methodology). Ultramafic rocks are characteristic of the Middle Nappe, but greenschist to lower amphibolite-grade clastic metasedimentary and calcareous psammitic rocks are the dominate rock types (Thorsnes and Løseth, 1991). Rocks of the Upper Nappe include late Cambrian to Ordovician calcareous psammites, pelitic schists, and migmatitic quartzofeldspathic to calc-silicate gneisses metamorphosed under upper amphibolite to granulite facies metamorphic conditions (Barnes et al., 2007, 2011).

Each of the broadly north-trending nappes has an aerial extent of tens to hundreds of kilometers; widths in map view range from 4 km to >50 km. Individual stratigraphic packages within each nappe extend several kilometers along strike, and range in thickness from tens of meters to several kilometers (Myrland, 1972; Dumond et al., 2005). Nappes are bounded by east-dipping shear zones with complex structural histories (Fig. 1; Yoshinobu et al., 2002).

### Andalshatten Batholith

The Helgeland Nappe Complex was intruded by the Ordovician–Silurian Bindal Batholith (Fig. 1). The Bindal Batholith is the largest Caledonian-aged batholith in Norway, and consists of a mosaic of more than 50 major intrusions spanning ages from ca. 480 to 425 Ma. The amalgamation of nappes within the Helgeland Nappe Complex and Bindal magmatism are the result of collision of arc terranes within the Iapetus Ocean during the early phases of the Ordovician–Silurian Caledonian orogeny (Yoshinobu et al., 2002; Roberts et al., 2002; Barnes et al., 2007). The Andalshatten batholith represents one of the last large additions to the crust in the Velfjord region (Fig. 1). Crystallization of magmas of the Andalshatten and other spatially and temporally related intrusions (e.g., Barnes and Prestvik, 2000) occurred at pressures between 600 and 800 MPa (Al-in-hornblende geobarometry; Yoshinobu et al., 2002).

The Andalshatten batholith (Fig. 2) is a large (322 $km^2$ map area, >700 $km^3$ in volume) high-potassium calc-alkaline (Nordgulen, 1993) composite intrusion and is composed of at least five distinctive mapped rock types (oldest to youngest based on crosscutting relationships): (1) schlieren-banded to gneissic granodiorite (~36 $km^2$, ~11% batholith area); (2) coarse-crystalline to megacrystic K-feldspar granodiorite (~221 $km^2$, ~69% of batholith area); (3) amphibole-bearing diorite (35 $km^2$, 11% batholith area); (4) hornblende biotite granite and minor two-mica leucogranite; and (5) tonalite (6 $km^2$, 2% of batholith area; area measurements of lithologies made at 1:12,000 scale using ArcGIS; http://www.esri.com/software/arcgis; Fig. 2). Metamorphic screens and xenoliths underlie 24.3 $km^2$, or 8% of the batholith area. The tonalite unit is an aerially extensive tabular body located in the southern portion of the batholith (Fig. 2) and is interpreted to be synmagmatic with the megacrystic granodiorite (Nordgulen et al., 1992). This body was not mapped during this

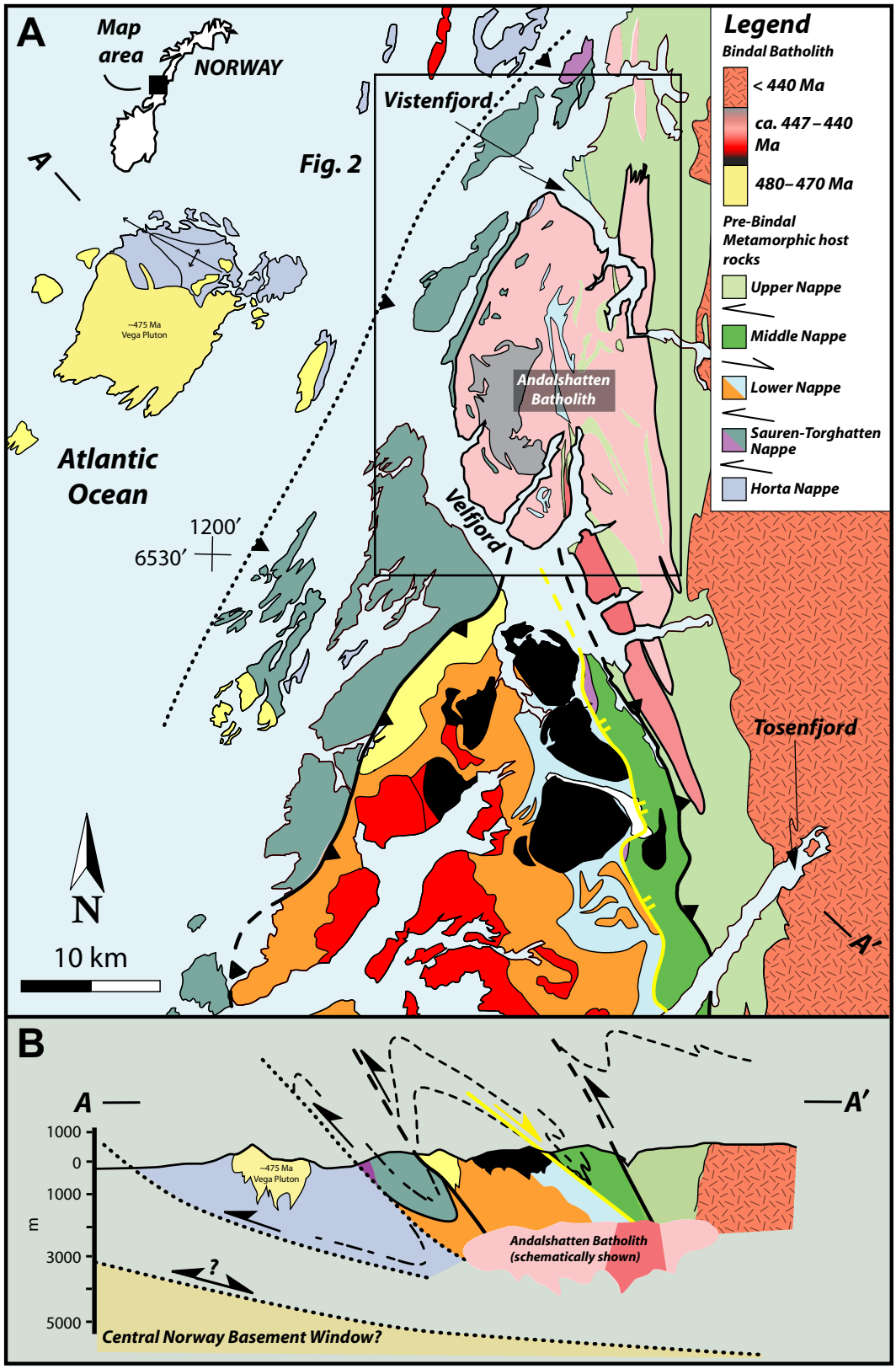


**Figure 1. (A) Tectonic map of the Helgeland Nappe Complex (HNC) and Bindal Batholith, central Norway. The ca. 442 Ma Andalshatten batholith intrudes four nappes within the HNC. (B) Schematic cross section illustrating crosscutting nature of Andalshatten batholith and nappes of the HNC.**

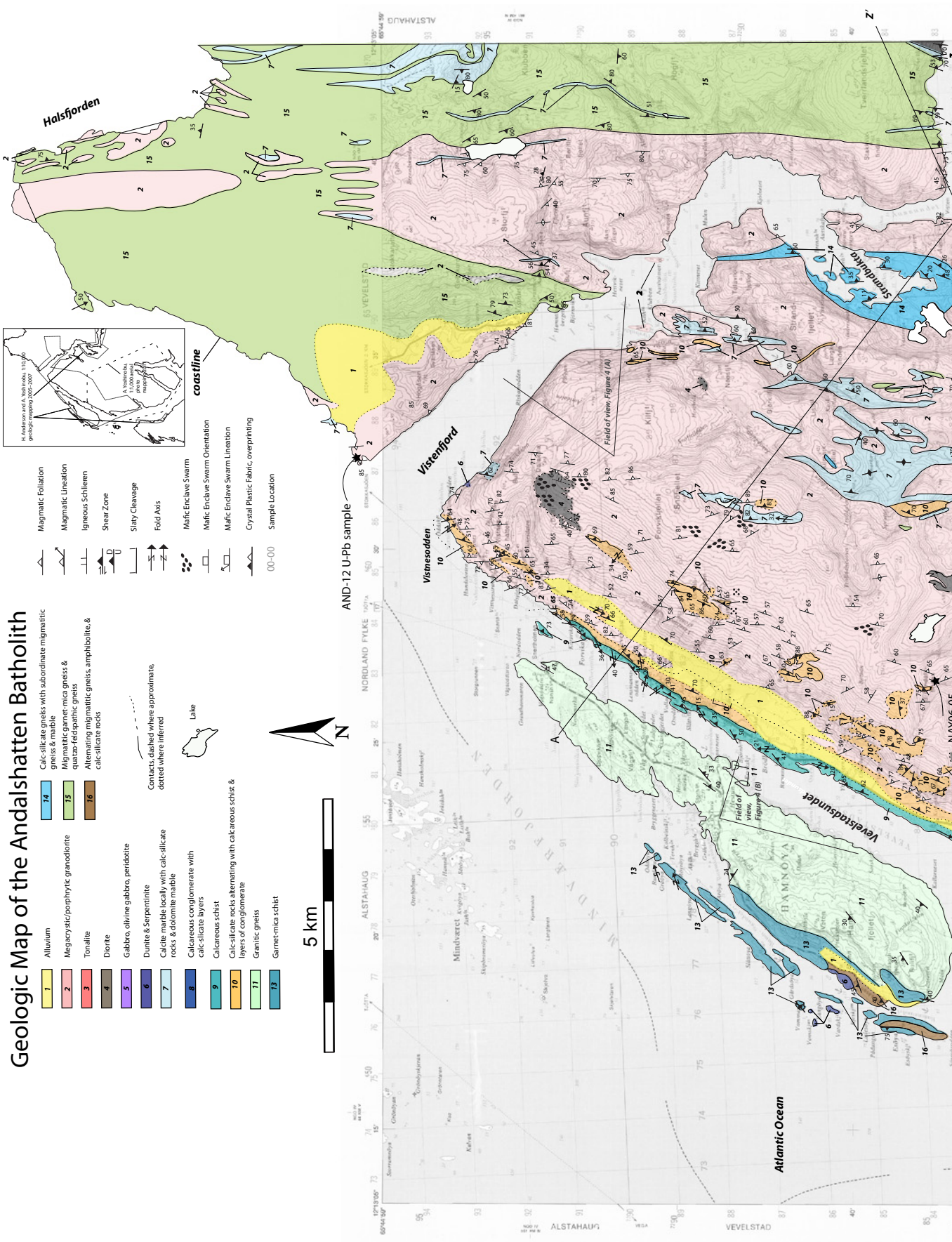


**Figure 2. Geologic map of the Andalshatten batholith. Geodetic datum: WGS84, UTM Grid, Zone 33, base map Vevelstad 1:50,000, Kartblad 1826 III. Base geologic map is from Nordgulen et al. (1992). Cross-section lines A–A′, B–B′, C–C′, D–D′, and E–E′ are in Figure 3. Cross-section line z–Z′ is in Figure 14.**

study and so is not described further. Published major and selected trace element data indicate that the batholith exhibits a northeast to southwest smooth variation from 58% $SiO_2$ to 70% $SiO_2$ (Nordgulen, 1993; Nordgulen et al., 1993). However, initial Sr and εNd isotopic data across these values of $SiO_2$ cluster around 0.70855 and –4 to –5, respectively (Nordgulen and Sundvoll, 1992; Nordgulen, 1993; Nordgulen et al., 1993). Based on map data from Figure 2 as well as detailed geologic mapping and outcrop studies presented in the following, five geologic cross sections across the batholith are shown in Figure 3 and display the general shape and nature of contacts in the subsurface and the orientation of structures within the contact aureole. Figure 4 displays four annotated panorama images of the outcrop nature and geometry of the batholith, including the northeastern apophasis, interlayered mafic and felsic bodies within the central portion of the batholith, and some of the kilometer-scale metamorphic screens.

Schlieren-banded to gneissic granodiorite occurs along the eastern margin of the batholith and is characterized by a hypidiomorphic, nonequigranular fabric that is commonly overprinted by a gneissic (i.e., subsolidus) fabric. This lithology is in sharp contact with deformed migmatite and pelitic schist of the Upper Nappe, along a north-south–trending, steeply dipping, and locally sheared intrusive contact (Figs. 2 and 3). The schlieren-banded to gneissic granodiorite unit contains felsic and mafic compositional layering defined by biotite-rich bands and is medium crystalline (1–5 mm) to porphyritic (Figs. 5A–5C). Sparse megacrysts of K-feldspar are observed within an equigranular matrix (e.g., Figs. 5B, 5C). Biotite-rich compositional banding and K-feldspar megacrysts define a foliation that is locally folded about steeply dipping, north-trending axial planes (Fig. 5B). Elsewhere along the eastern contact, this fabric is defined by recrystallized tails of feldspar, quartz, and biotite that overprint a probable magmatic foliation defined by aligned K-feldspar megacrysts (our data; Nordgulen et al., 1992). The overprinting crystal-plastic fabric displays pluton-up, host rock–down shearing, and cuts hypersolidus (i.e., magmatic) shear bands that exhibit similar kinematics (red arrows in Figs. 5A, 5C).

Coarse-crystalline to megacrystic K-feldspar granodiorite is the most abundant rock type and underlies >69% of the exposed area (Figs. 2 and 5D–5F). Along the eastern side of the pluton, megacrystic granodiorite is in sharp, sheeted, and gradational contact with the schlieren-banded to gneissic granodiorite. Along the western pluton margin, megacrystic granodiorite discordantly cuts calc-silicate host rocks along a moderate to steeply east dipping curviplanar contact (Figs. 2, 3, and 4). A moderate to well-developed magmatic foliation is defined by subparallel megacrysts of K-feldspar and hornblende. The magmatic foliation is locally overprinted by a subparallel crystal-plastic metamorphic fabric within a few meters of xenoliths in the western portions of the pluton (see following).

Amphibole-bearing diorite crops out as massive kilometer-scale intrusions within the porphyritic granodiorite and meter to submeter-scale microgranitoid enclaves and enclave swarms (Fig. 6). The largest of the dioritic bodies is ~35 $km^2$ and is located within the southwestern part of the pluton (Figs. 2, 3, and 4). Along the southwestern margin of the diorite, contacts show a nonuniform gradation from megacrystic granodiorite to diorite. Lobate and undulating contacts between the diorite and the granodiorite are common (Fig. 6A). Along the western contact of the large diorite body (Fig. 2), several-meters-thick, east-dipping sheets of diorite and

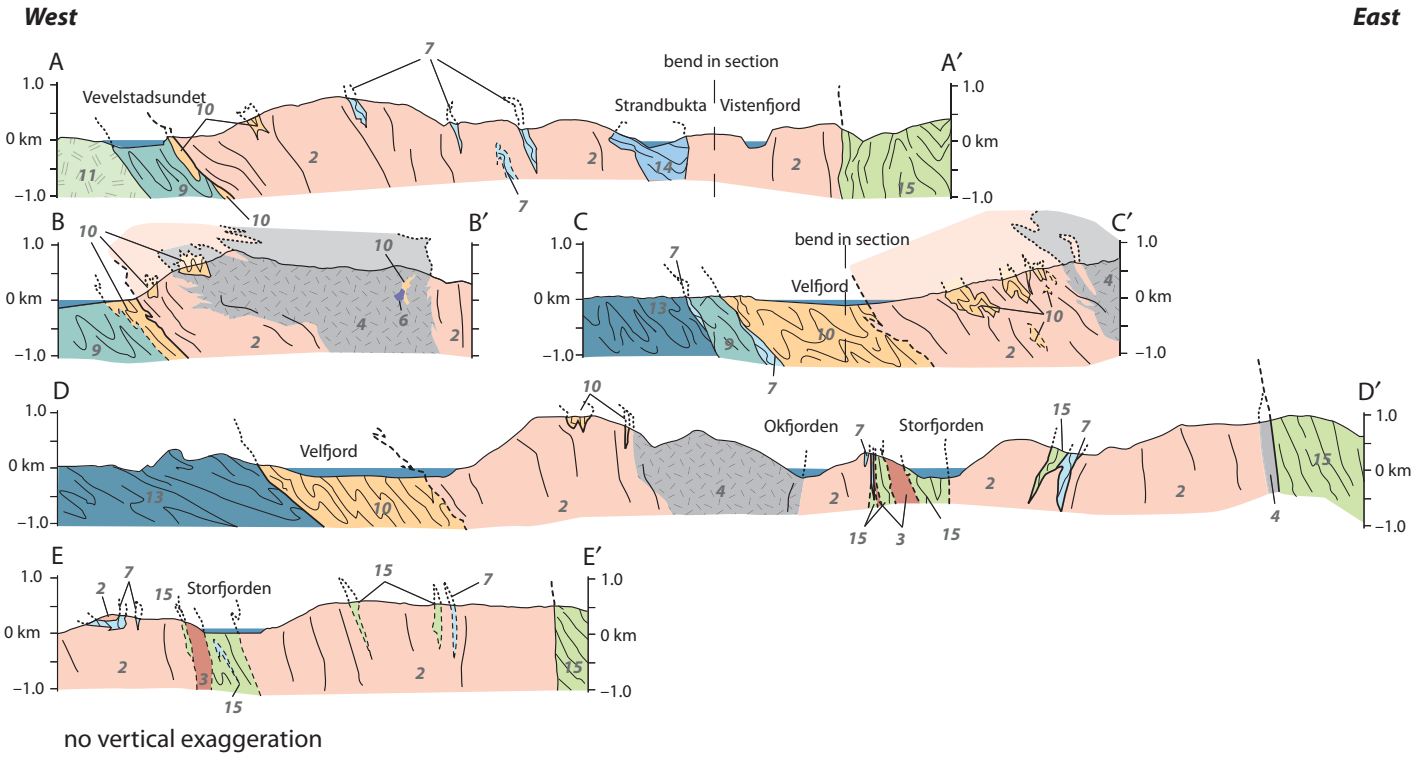


**Figure 3. Five geologic cross sections across the Andalshatten batholith; sections lines are in Figure 2. Major fjords intersected by cross-section lines are noted. Colors and numbers correspond to legend in Figure 2. No vertical or horizontal exaggeration. Interpreted intrusive contact geometries between large screens, granodiorite, and diorite are projected above ground and are illustrated with slightly transparent colors and dashed lines in cross-sections B–B′ and C–C′. Fine, wavy lines in metamorphic rocks and igneous rocks are metamorphic and magmatic foliation trends, respectively.**

granodiorite are sandwiched together. Evidence of larger scale granodiorite and/or diorite sheeting is shown in Figure 4. Flame-type structures and pipe-like tubes of granodiorite that appear to have intruded perpendicular to the base of the overlying diorite sheets indicate a paleo-up direction (Fig. 6A; e.g., Wiebe and Collins, 1998). Centimeter-scale discontinuous sheeting or banding of these rock types is also observed within the interior of the massive diorite. Similar contact relations are observed for smaller diorite bodies in the central and northern part of the map area (Fig. 2). The basal layers of diorite generally dip shallowly to steeply east; the western contact of the large diorite body in Figure 2 has a variable dip from ~45° east at the highest exposures (e.g., Fig. 4D) to subvertical at sea level (Fig. 2), indicative of an anvil-shaped intrusion in cross section (e.g., Fig. 3B).

Fine- to medium-crystalline microgranitoid enclaves of dioritic composition are commonly observed in outcrop-scale swarms within close proximity to massive dioritic bodies and metamorphic screens, but are also unevenly distributed within the pluton. Figure 6B displays a spectacular cliff-face exposure of a microgranitoid enclave swarm located on the structural top of a large calc-silicate screen. This ~8-m-thick swarm has a strike length of >50 m, and occurs over the jagged intrusive contact of the screen. Long axes of individual enclaves are subparallel to the contact with the underlying screen. Where not observed adjacent to large metamorphic screens, individual enclaves are generally elongate subparallel to the magmatic foliation of the megacrystic granodiorite (Fig. 6C). K-feldspar phenocrysts may be entirely enclosed (e.g., Fig. 6D) or partially entrained in the enclaves (e.g., Fig. 6E). Enclave swarms sometimes are strongly flattened in the plane of the swarm with individual enclave axial ratios >4:1. These enclaves display evidence for physical mingling of mafic magmas and entrained K-feldspar phenocrysts presumably from the host granodioritic magma (Figs. 6E, 6F). Both massive diorite units shown in Figure 2 are interpreted to be comagmatic with the granodiorite based on these relationships.

Hornblende biotite granite crops out as dikes, sills, and meter-scale pods at and near the contacts of calc-silicate metasedimentary rocks and granodiorite. These fine-grained, equigranular intrusions range from 1 to 3 m wide and cut across xenoliths and screens. Magmatic fabric development within the granite is absent or parallel to the fabric within the adjacent granodiorite. Angular blocks of hornblende biotite granite are locally preserved as cognate xenoliths within the granodioritic phase of the pluton (see following).

## Geochronology

Chemical abrasion–thermal ionization mass spectrometry (CA-TIMS) U-Pb zircon and titanite ages of two granodioritic samples were determined for this study, including sample AND-12, from the northwestern tip of the pluton, and sample NAY06–05, from the interior of the pluton (Fig. 2). For the methodology and other analytical details, including images of the analyzed zircons (Figs. A1, A2) and concordia plots (Figs. A3, A4), see the Supplemental File[1].

Sample AND-12 is a megacrystic granodiorite containing quartz, plagioclase, K-feldspar, and biotite, with lesser amounts of epidote, muscovite, and titanite. A weak magmatic fabric within this sample is defined by sparse K-feldspar megacrysts. Crystal-plastic deformation overprints the magmatic fabric and is defined by grain boundary migration recrystallization of quartz and minor recrystallization (subgrain development) of feldspar. In thin section, a seriate crystal size distribution is observed along with K-feldspar megacrysts, recrystallized quartz aggregates, and interstitial biotite. Zircons separated from this sample were uniformly euhedral and yellow, and ranged in size from 50 μm in length to >350 μm (Fig. A1 in the Supplemental File [see footnote 1]). Many grains appeared cracked and therefore were not analyzed. The clearest grains were selected for analysis to minimize inclusion of even minor inherited components. The grains were mechanically abraded to remove metamict rims and any possible metamorphic overgrowths, then annealed and dissolved in steps following the chemical abrasion method of Mattinson (2005). Titanite crystals within this sample were both dark and pale.

Sample NAY06–05 is a porphyritic granodiorite containing quartz, plagioclase, K-feldspar, and biotite with lesser amounts of hornblende, epidote, and titanite. In outcrop, the magmatic fabric is recognized by sparse elongate crystals of feldspar. The primary fabric is more clearly observed in thin section and is defined by blocky and elongate crystals of feldspar and elongate quartz. Zircons separated from this sample were euhedral and yellow, with almost all zircon grains containing cracks and internal defects, although no older cores were visible. Grains ranged in length from 50 μm to >350 μm. All but two of the analyzed grains were mechanically abraded to remove metamict rims and any possible metamorphic overgrowths. Seven large single grains and two multigrain fractions were analyzed for sample NAY06–05. Figure A2 in the Supplemental File (see footnote 1) displays representative zircon grain images for sample NAY06–05.

The CA-TIMS method of zircon analysis works to remove domains within the zircon grain that have undergone Pb loss, yielding more accurate and less discordant dates (Mattinson, 2005) by dissolving metamict high-U domains and nonmetamict low-U domains separately (e.g., Schoene et al., 2006) (see the Supplemental File [see footnote 1] for details). The weighted mean $^{206}Pb/^{238}U$ date for sample AND-12 is 442.67 ± 0.14 Ma, whereas the date for sample NAY06–05 is 441.53 ± 0.40 Ma. Titanite analyses yielded dates of 441.30 ± 0.21 Ma for sample AND-12 and 436.10 ± 2.80 Ma for sample NAY06–5. Analytical results are reported in Table 1 and shown on concordia diagrams (Figs. A3 and A4 in the Supplemental File [see footnote 1]).

CA-TIMS zircon dates yield a resolvable difference between the magmatic ages of the two samples. Comparisons between the $^{206}Pb/^{238}U$ weighted average dates of 442.67 ± 0.14 Ma and 441.53 ± 0.40 Ma are interpreted to indicate a difference in magmatic ages of between 0.6 and 1.68 Ma at 95% confidence limits. These dates are interpreted to reflect discrete pulses of magmatism very close in time within the granodioritic unit of the Andalshatten batholith. The titanite ages are <1 to ~6 Ma younger than the zircon ages and are discussed in the following.

## Host Rock Geology and Structure

The Andalshatten batholith truncates discordantly the four nappes of the Helgeland Nappe Complex along the inferred southern contact (Figs. 1 and 2). Along its western margin, the batholith intrudes the Sauren-Torghatten Nappe, whereas the eastern contact juxtaposes the batholith with the Upper Nappe (Figs. 1 and 2). To the north of the batholith, host rock tectonostratigraphy is dominated by pelitic migmatite and calcareous rocks tentatively correlated with the Upper Nappe (Nordgulen et al., 1992; Yoshinobu et al., 2002; this study; Figs. 2 and 3). Therefore, the batholith was assembled across a structural culmination of the four nappes within the Helgeland Nappe Complex. The various lithologies that compose the four nappes in the hot rocks can be traced along strike into the batholith, where they occur as xenoliths and screens that define a ghost stratigraphy (Fig. 1). The ghost stratigraphy is discussed further in the following sections.

[1]Supplemental File. Word file of geochronology methods. If you are viewing the PDF of this paper or reading it offline, please visit http://dx.doi.org/10.1130/GES00824.S1 or the full-text article on www.gsapubs.org to view the Supplemental File.

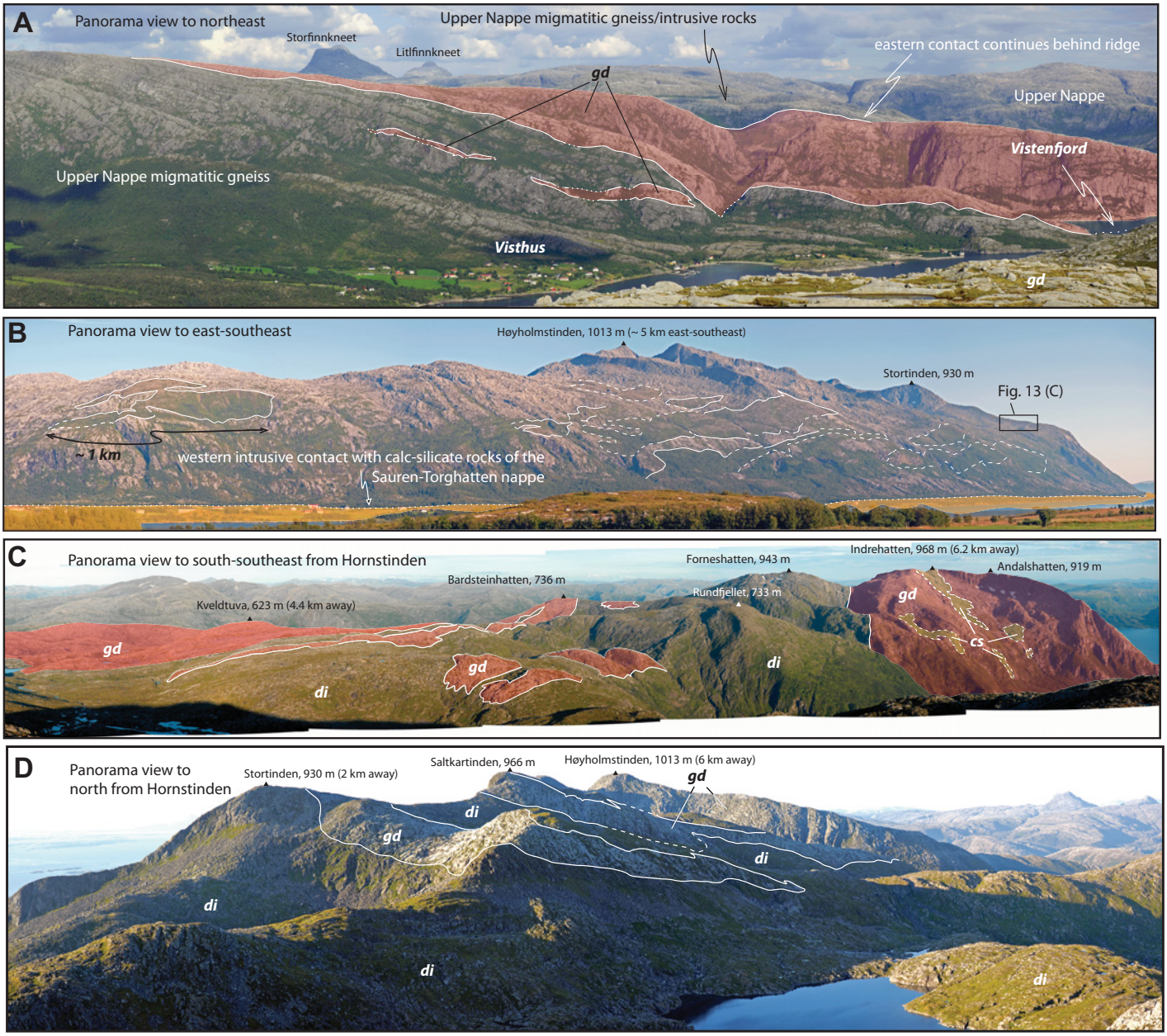


**Figure 4. Panorama images of the Andalshatten batholith. See Figure 2 for location and perspective for each image. (A) View to the northeast of the elongate geometry of the northeastern apophasis of the Andalshatten batholith (gd). (B) View to the east-southeast from the island of Hamnøya of the largest screens contained within the granodioritic phase; northernmost screen (left) is ~1 km long. (C) View to south-southeast from Hornstinden of intrusive relations between granodiorite and diorite (di) phases. Note calc-silicate (cs) screens contained within the granodiorite, the largest of which is ~1.5 km in long dimension. (D) View to north from Hornstinden displaying sheeted nature of mutually intruded granodiorite and diorite. Colors correspond to Figure 2.**

Outside of the 1-km-wide contact aureole to the west, the dominant macroscopic planar structure in the host rocks is a relict sedimentary bedding-parallel foliation, $S_b$, and transposed regional foliation, $S_T$, developed within rocks of the Sauren-Torghatten Nappe (terminology following Tobisch and Paterson, 1988; Nordgulen et al., 1992). Equivalent structures in the Vega archipelago to the west and south (Fig. 1) were described in Marko (2012), Marko et al. (2005), Oalmann et al. (2011), and Anderson et al. (2005). Within the Horn peninsula to the southwest (see Fig. 2), metamorphic foliations developed in calc-silicate schists and marbles display variable orientations, with strikes ranging from east-west to north-south and less variable dip angles from 50° to 75° east (Fig. 2). These metamorphic foliations define a tight map-scale fold with an axial plane that is oblique and discordant to the western margin of the Andalshatten batholith (Fig. 2).

Two sets of pre-emplacement folds occur within the host rocks to the west and south of the batholith. The first, and older set, include intrafolial, centimeter-scale isoclinal folds. These

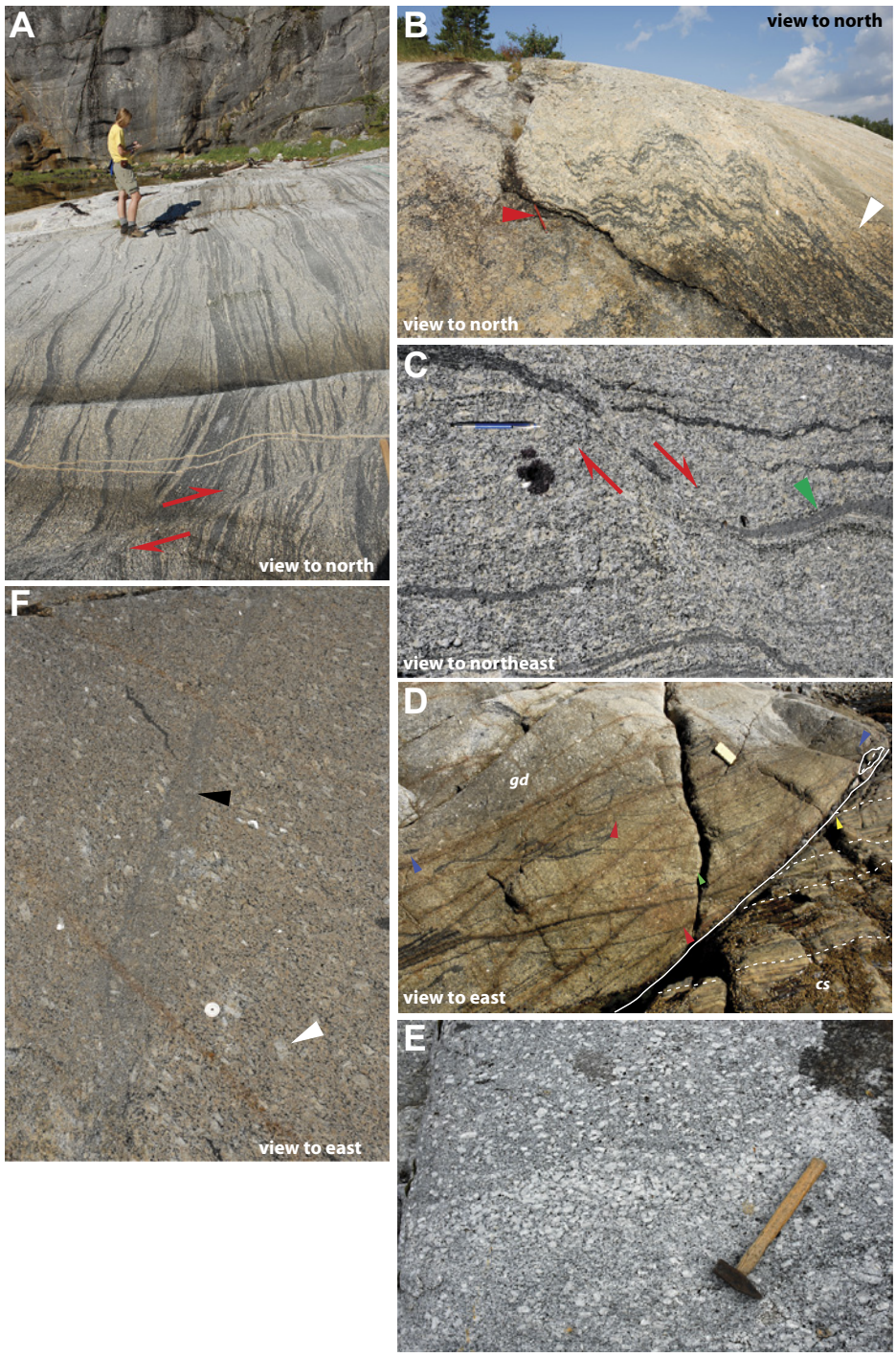


**Figure 5. Felsic lithologies of the Andalshatten batholith. (A) Schlieren-banded to gneissic granodiorite. Red arrows indicate top-to-the-east magmatic shear band. (B) Folded schlieren banding in porphyritic to K-feldspar megacrystic (white arrow) granodiorite. Pencil for scale (red arrow). (C) Down-to-the-east magmatic shear band (red arrows) cutting schlieren-banded and gneissic granodiorite and elongated mafic magmatic enclaves (green arrow); pencil for scale. (D) Contact of porphyritic and K-feldspar megacrystic granodiorite (gd) and western calc-silicate (cs) host rocks (white bold line). Bedding in host rocks is decorated with white dashed lines. Note contact-bedding cut-offs (yellow arrows). Disc-shaped mafic magmatic enclaves (10 cm; blue arrows) are subparallel to magmatic foliation defined by K-feldspar megacrysts. Red arrows point to truncation surfaces of convex schlieren bands that bow toward the contact. (E) K-feldspar megacrystic granodiorite. Note variable amounts of megacrysts and increased mafic component in upper half of outcrop. Megacrysts define a strongly developed magmatic foliation subparallel to the long dimension of the image. (F) K-feldspar megacrystic granodiorite with magmatic foliation trending from lower right to upper left (white arrow). The black arrow denotes a fine-crystalline K-feldspar porphyritic dike with diffuse boundaries that crosscuts the granodiorite.**

folds and the $S_b$ foliations are folded about meter- to outcrop-scale broad to isoclinal similar folds. Axial planes to these outcrop-scale folds and isoclinal fold limbs strike broadly north-northeast and dip moderately eastward. The axial planes and limbs of the outcrop-scale folds are broadly subparallel to the transposed foliation ($S_T$). Because of the discordant nature of the trends of metamorphic foliations within the Horn peninsula and the intrusive contact (see Fig. 2), it is likely that these rocks are not within the contact aureole. Foliations within the host rocks, screens, and xenoliths are generally north-northeast striking with steep east dips, whereas linear structures show a broad spectrum of northeast and south-plunging attitudes (Fig. 7). Linear features within the screens and xenoliths form a tighter distribution with broadly north and south trends, but are dominantly north-plunging (Fig. 7B).

## Contact Aureole

A contact aureole (to 1 km wide) surrounding the batholith may be defined along the western margin based on a change in morphology and geometry of preexisting structures and a general increase in the degree of deformation in calc-silicate rocks. Lesser amounts of marble and minor psammitic rocks occur within the structural aureole. Metamorphic index miner-

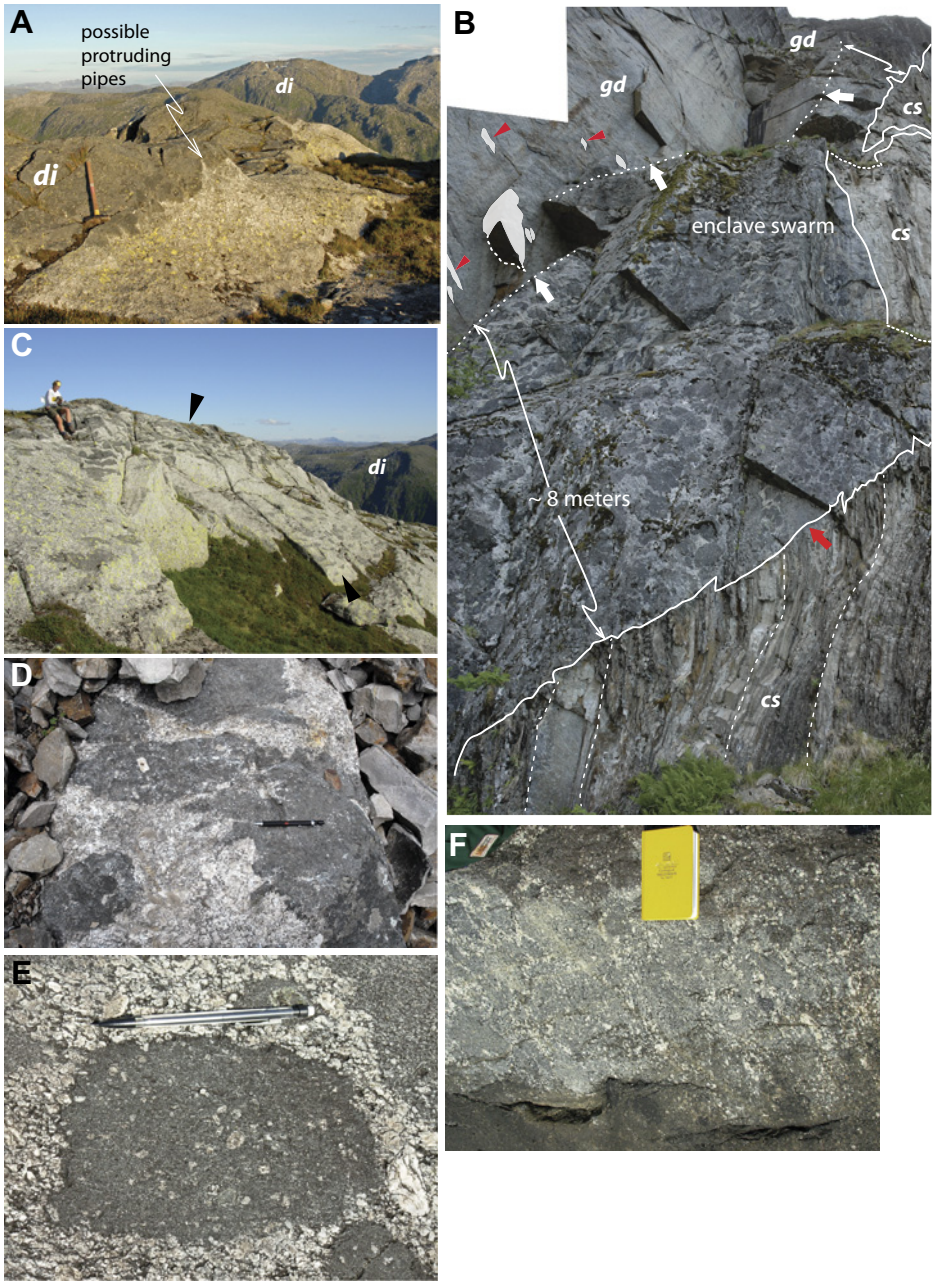


**Figure 6. Diorite of the Andalshatten batholith. (A) Lobate contact of pyroxene diorite and underlying granodiorite with pipes of granodiorite protruding into diorite (di). (B) Swarm of disc-shaped microgranitoid enclaves ~8 m thick in matrix of porphyritic granodiorite resting above the structural top of calc-silicate screen (cs) (V screen; see text for details). Red arrow points to jagged contact. White arrows and dotted lines indicate approximate boundary of swarm, above which is porphyritic granodiorite (gd) with a few conspicuous microgranitoid enclaves (red triangles). (C) Enclave swarm in granodiorite. (D) Mingling of diorite and granodiorite and preservation of K-feldspar megacryst in enclave. (E) Enclave with K-feldspar phenocrysts dispersed throughout the enclave and along contact with granodiorite. (F) Mingle zone of deformed enclaves and granodiorite; such outcrops preserve physical evidence for the mechanical mingling of K-feldspar megacrysts and mafic magmas.**

als are not well developed in the host rocks; the local presence of garnet, sillimanite, and hornblende in appropriate lithologies is consistent with amphibolite facies conditions attending dynamothermal contact metamorphism. The width of the contact aureole along the eastern margin is not well established. This is due in part to the relatively high metamorphic grade of the host rocks (sillimanite-bearing, regional pelitic migmatite) into which the batholith intruded (Nordgulen et al., 1992).

Within the western contact aureole, regional planar and linear structures are steep and aligned subparallel to the arcuate batholith contact (Figs. 2 and 3). Pre-emplacement fold axes and lineations define two weak maxima in the northeastern and southern portions of a stereonet projection (Fig. 7B). Folds concentrated in the north-plunging domain are mainly found along the southwestern pluton margin, whereas folds concentrated in the south-plunging domain are dominantly found along the northwestern pluton margin. Along the northwest contact of the batholith at Vistnesodden (Fig. 2), west-directed protomylonitic fabrics, including S-C fabrics, overprint east-dipping magmatic foliations. These rocks display asymmetric, recrystallized feldspar mantles surrounding cores of K-feldspar, indicative of moderately high temperature subgrain-rotation recrystallization (e.g., Vernon, 2004). This deformation is consistent with batholith-up, host rock–down kinematics, and is similar to the structural sequence and kinematics described previously for the eastern contact, i.e., batholith-up, host rock–down shearing during emplacement, solidification, and cooling (see Fig. 5).

Along the southwestern contact, a zone of spectacular emplacement-related deformation is characterized by preexisting fold and foliation reactivation and intrusion of dikes of granodiorite (see also Yoshinobu et al., 2009).

TABLE 1. U-Pb CHEMICAL ABRASION–THERMAL IONIZATION MASS SPECTROMETRY (CA-TIMS) ZIRCON DATA

| Sample | Weight (µg) | U (ppm) | Sample Pb (pg) | Pb (ppm) | Initial Pb (pg) | $\frac{Pb^*}{Pbc}$ | $\frac{^{206}Pb}{^{204}Pb}$ | $\frac{^{206}Pb}{^{208}Pb}$ | $\frac{^{206}Pb}{^{238}U}$ (rad.) | $\frac{^{206}Pb}{^{238}U}$ %err | $\frac{^{207}Pb}{^{235}U}$ (rad.) | $\frac{^{207}Pb}{^{235}U}$ %err | $\frac{^{207}Pb}{^{206}Pb}$ (rad.) | $\frac{^{207}Pb}{^{206}Pb}$ %err | 206/238 Age (Ma) | err | 207/235 Age (Ma) | err | 207/206 Age (Ma) | err | Rho | % disc. |
|---|---|---|---|---|---|---|---|---|---|---|---|---|---|---|---|---|---|---|---|---|---|---|
| **AND-12 Andalshatten megacrystic granodiorite (UTM 33 W 387170 E, 7294653 N)** | | | | | | | | | | | | | | | | | | | | | | |
| cl aa lg sD | 5.88 | 634 | 46.2 | 272 | 0.82 | 4.8 | 32.3 | 3494 | 8.76 | 0.07116 | –0.07 | 0.54789 | –0.14 | 0.05584 | –0.11 | 443.15 | ±0.30 | 443.61 | ±0.61 | 445.98 | ±2.49 | 0.58 | 0.66 |
| cl aa lg sA* | 8.5 | 806 | 57 | 485 | 0.21 | 1.8 | 91.5 | 17190 | 10.34 | 0.07111 | –0.12 | 0.54725 | –0.15 | 0.05581 | –0.09 | 442.84 | ±0.52 | 443.19 | ±0.66 | 445.01 | ±2.01 | 0.8 | 0.5 |
| cl aa sm pk2 3gr* | 6.94 | 948 | 68.1 | 472 | 1.15 | 8 | 40.8 | 3730 | 10.07 | 0.07111 | –0.07 | 0.54774 | –0.11 | 0.05587 | –0.08 | 442.82 | ±0.29 | 443.52 | ±0.48 | 447.1 | ±1.86 | 0.64 | 0.99 |
| cl aa lg sB* | 7.9 | 529 | 38.2 | 302 | 0.72 | 5.7 | 32.5 | 3337 | 9.66 | 0.07109 | –0.12 | 0.54733 | –0.19 | 0.05584 | –0.14 | 442.7 | ±0.55 | 443.25 | ±0.83 | 446.05 | ±3.01 | 0.69 | 0.78 |
| cl aa lg sE* | 4.7 | 690 | 48.7 | 229 | 0.15 | 0.7 | 54.1 | 20384 | 10.53 | 0.07109 | –0.05 | 0.54673 | –0.11 | 0.05578 | –0.09 | 442.69 | ±0.21 | 442.85 | ±0.50 | 443.69 | ±2.07 | 0.57 | 0.23 |
| cl aa lg sC* | 7.9 | 533 | 37.8 | 298 | 0.61 | 4.8 | 35.5 | 3944 | 11.67 | 0.07104 | –0.07 | 0.54675 | –0.14 | 0.05582 | –0.11 | 442.4 | ±0.30 | 442.86 | ±0.60 | 445.29 | ±2.46 | 0.58 | 0.67 |
| dk tnt sA | 557 | 55 | 4.72 | 2632 | 1.05 | 586 | 3.4 | 250 | 5.34 | 0.07085 | –0.05 | 0.54374 | –0.18 | 0.05566 | –0.16 | 441.3 | ±0.21 | 440.89 | ±0.78 | 438.75 | ±3.61 | 0.43 | –0.6 |
| *Zircon crystallization age = 441.53 ± 0.40 Ma (MSWD = 3.4) 4 point* weighted 206Pb/238U date* | | | | | | | | | | | | | | | | | | | | | | |
| **NAY06-05 Andalshatten coarse-grained granodiorite (UTM 33 W 382366 E,7283612 N)** | | | | | | | | | | | | | | | | | | | | | | |
| ck aa xl sB | 15.9 | 577 | 41.3 | 656 | 0.77 | 12.2 | 41 | 3401 | 11.5 | 0.07144 | –0.06 | 0.54985 | –0.1 | 0.05582 | –0.08 | 444.82 | ±0.28 | 444.9 | ±0.45 | 445.29 | ±1.73 | 0.65 | 0.11 |
| ck aa xl sA | 21 | 1101 | 81.1 | 1704 | 2.94 | 61.7 | 25 | 1700 | 9.54 | 0.07116 | –0.3 | 0.54826 | –0.32 | 0.05588 | –0.11 | 443.13 | ±1.31 | 443.86 | ±1.40 | 447.65 | ±2.40 | 0.94 | 1.05 |
| ck aa xl p1 6gr | 26 | 427 | 30.1 | 782 | 0.06 | 1.5 | 156 | 33324 | 10.61 | 0.07112 | –0.07 | 0.54749 | –0.09 | 0.05583 | –0.07 | 442.92 | ±0.29 | 443.35 | ±0.42 | 445.57 | ±1.50 | 0.7 | 0.61 |
| cl aa lg p2 3gr | 15.5 | 341 | 24.4 | 378 | 0.18 | 2.9 | 59 | 8320 | 9.46 | 0.0711 | –0.07 | 0.54672 | –0.11 | 0.05577 | –0.09 | 442.78 | ±0.29 | 442.85 | ±0.50 | 443.2 | ±1.92 | 0.64 | 0.1 |
| ck aa xl sE | 7.9 | 314 | 23.5 | 186 | 1.43 | 11.3 | 12 | 1001 | 10.55 | 0.07098 | –0.05 | 0.5461 | –0.15 | 0.0558 | –0.13 | 442.07 | ±0.23 | 442.44 | ±0.67 | 444.38 | ±2.92 | 0.53 | 0.54 |
| ck aa xl sG* | 5.3 | 290 | 20.8 | 110 | 0.21 | 1.1 | 18 | 6168 | 9.14 | 0.07094 | –0.07 | 0.54524 | –0.28 | 0.05575 | –0.25 | 441.79 | ±0.32 | 441.87 | ±1.24 | 442.3 | ±5.45 | 0.6 | 0.12 |
| ck xl sC* | 35 | 444 | 31.4 | 1099 | 0.02 | 0.6 | 267 | 112685 | 9.84 | 0.07093 | –0.07 | 0.54564 | –0.09 | 0.05579 | –0.07 | 441.79 | ±0.30 | 442.14 | ±0.42 | 443.97 | ±1.46 | 0.72 | 0.51 |
| ck xl sD* | 33 | 442 | 31.1 | 1028 | 0.01 | 0.5 | 188 | 140294 | 10.03 | 0.07087 | –0.06 | 0.54502 | –0.08 | 0.05577 | –0.06 | 441.41 | ±0.25 | 441.73 | ±0.36 | 443.41 | ±1.28 | 0.7 | 0.47 |
| ck aa xl sF* | 15.9 | 284 | 20.7 | 328 | 0.65 | 10.4 | 21 | 1960 | 9.91 | 0.07085 | –0.06 | 0.54544 | –0.12 | 0.05583 | –0.1 | 441.29 | ±0.26 | 442 | ±0.55 | 445.71 | ±2.28 | 0.58 | 1.02 |
| dk cl tnt sA | 214 | 124 | 9.49 | 2031 | 1.32 | 283 | 5.8 | 436 | 34.05 | 0.07047 | –0.15 | 0.53999 | –0.22 | 0.05558 | –0.15 | 438.98 | ±0.65 | 438.42 | ±0.96 | 435.52 | ±3.38 | 0.72 | –0.82 |
| dk pc tnt sB | 87.9 | 206 | 17.8 | 1563 | 4.43 | 390 | 2.8 | 224 | 51.62 | 0.07026 | –0.06 | 0.53892 | –0.27 | 0.05563 | –0.24 | 437.71 | ±0.27 | 437.71 | ±1.17 | 437.69 | ±5.43 | 0.48 | –0.01 |
| *Zircon crystallization age = 442.67 ± 0.14 Ma (MSWD = 1.17) 5 point* weighted 206Pb/238U date* | | | | | | | | | | | | | | | | | | | | | | |

*Note:* Locations in Universal Transverse Mercator coordinates. Sample abbreviations: cl—clear, ck—cracked, aa—mechanically air abraded, lg—large, sm—small, xl—extra large, euh—euhedral, dk—dark, pc—polycrystalline, tnt—titanite, s—single grain, gr—number of grains, pk—pick identifier, *—used in weighted mean.

Weight: represents estimated weight prior to first step of CA-TIMS dissolution for zircons. U and Pb concentrations are based on this weight and the U and Pb atoms measured from the second dissolution step only. The U and Pb concentrations may be underestimations for zircons, depending on how much material was dissolved and leached in the first step. They are useful for internal comparisons, however. Picograms (pg) sample and initial Pb from the second dissolution step are measured directly.

Sample Pb—sample Pb (radiogenic + initial) corrected for laboratory blank; Initial Pb—common Pb corrected for laboratory blank of 3.5 pg Pb for zircon analyses, 20 pg Pb for titanite; Pb*/Pbc—radiogenic Pb to total common Pb (blank + initial); Corrected atomic ratios—$^{206}Pb/^{204}Pb$ corrected for blank, mass discrimination and tracer, all others corrected for blank, mass discrimination, tracer and initial Pb, values in parentheses are 2 sigma errors (err; in %); Rho—$^{206}Pb/^{238}U$ vs $^{207}Pb/^{235}U$ error correlation coefficient; % disc.—percent discordant.

Zircon and titanite dissolution and chemistry were adapted from methods developed by Krogh (1973), Parrish et al. (1987), and Mattinson (2005). All zircons were chemically abraded (CA-TIMS). Final dissolutions were spiked with a mixed $^{205}Pb/^{233}U/^{235}U$ tracer (ET535). Pb and U samples were loaded onto single rhenium filaments with respectively; isotopic compositions were measured in multicollector, static mode on a Micromass Sector 54 mass spectrometer at the University of Wyoming with 204Pb in Daly-photomultiplier collector and all other isotopes in Faraday collectors. Mass discrimination of 0.072 ± 0.04 %/amu for Pb was determined by replicate analyses of NIST SRM 981. U fractionation was determined internally during each run. Procedural blanks averaged 3.5 pg Pb for zircon and 20 pg Pb for titanite. Isotopic composition of the Pb blank was estimated as 19.09 ± 0.2, 15.652 ± 0.2, and 38.81 ± 0.2 for 206/204, 207/204 and 208/204, respectively. U blanks were consistently <0.6 pg. Concordia coordinates, intercepts, and uncertainties were calculated using MacPBDAT and ISOPLOT programs (based on Ludwig 1988, 1991); initial Pb isotopic compositions were estimated by average values from 9 galena analyses of the Langkilen sulfide ore deposit (18.312 ± 0.071, 15.609 ± 0.036, 38.117 ± 0.120 for 206/204, 207/204, 208/204, respectively; Birkeland et al., 1993). The decay constants used by MacPBDAT are those recommended by the I.U.G.S. Subcommission on Geochronology (Steiger and Jäger, 1977): 0.155125 x 10–9/yr for $^{238}U$, 0.98485 x 10–9/yr for $^{235}U$ and present-day $^{238}U/^{235}U$ = 137.88. MSWD is mean square of weight deviates.

Figure 8 displays outcrop-scale geologic maps of the complex deformation that characterizes the contact aureole in this region. In Figure 8A, a decreasing strain gradient exists in which preexisting upright folds of the transposed $S_T$ fabric are tight to isoclinal within 1–2 m of the pluton contact and become tight to open further west of the contact, away from the batholith margin. Similarly, several hundred meters to the north (e.g., Figs. 8B, 8C), axial planes of the $S_T$ fold generation are refolded with tight interlimb angles and anastomosing axial planes. These refolded structures are observed everywhere along the western pluton margin and are generally oriented subparallel to the bow-shaped western contact of the batholith (Fig. 2). However, the anastomosing axial planes and attenuated fold limbs adjacent to the batholith margin are both concordant and discordant along strike with intrusive contacts (Fig. 8C). Granite and granodioritic dikes are folded and have undergone boudinage within the plane of the reactivated axial planar ($S_T$) foliation (e.g., Figs. 8A, 8B). These features are only observed in the innermost aureole within 10–80 m of the batholith contact and are interpreted to be the result of synkinematic intrusion of dikes during aureole deformation. Although the reactivated metamorphic foliation and axial planes and limbs of folds within the contact aureole are broadly subparallel to the batholith contact, local truncations indicate that emplacement-related ductile strains and brittle elastic deformation occurred during dynamothermal contact metamorphism (Fig. 8; see following).

## Xenoliths and Screens Within the Andalshatten Batholith

The Andalshatten batholith is replete with metamorphic xenoliths and screens that underlie ~24 km$^2$, or 8% of the total batholith area (Fig. 2). In this report, xenoliths are defined as fragments of metamorphic rock contained within an intrusion; such rocks may be related to the currently exposed host rocks. Cognate xenoliths (or autoliths; e.g., Balk, 1937; Shane et al., 2012) represent fragments of related, earlier crystallized igneous rock now incorporated into the intrusion. Xenoliths, however, are distinguished from microgranitoid enclaves (e.g., Vernon et al., 1988; Didier and Barbarin, 1991) in that microgranitoid enclaves are interpreted to be comagmatic dioritic magmas that mingled with the host magma. Xenocrysts represent fragments of mineral phases that have been incorporated into the host igneous rock and may have originated from the metamorphic host rocks or from earlier, crystallized portions of the igne-

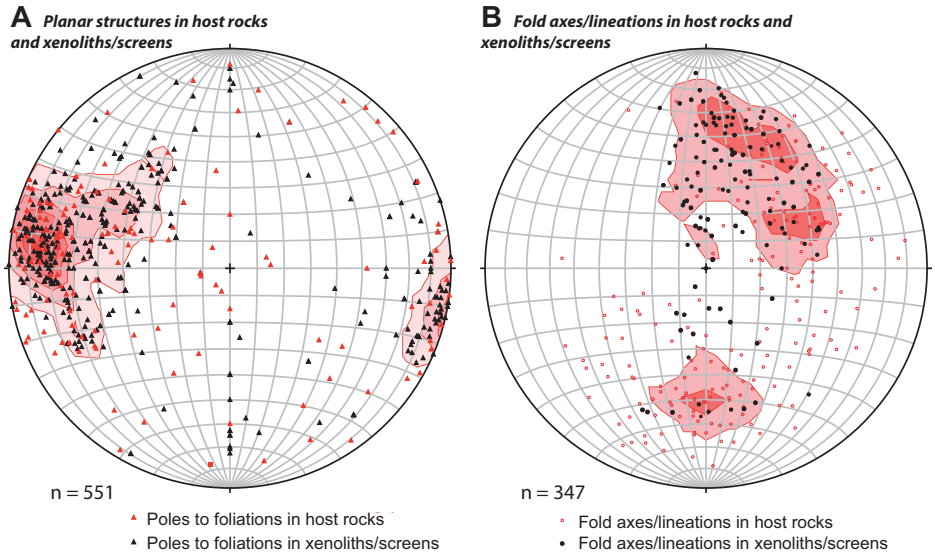


**Figure 7. Equal-area, lower hemisphere stereonets displaying planar and linear data for the host rocks of the Andalshatten batholith. (A) Poles to metamorphic foliations in host rocks (red triangles) and xenoliths and/or screens (black triangles). Contours include all planar data. (B) Fold axes and lineations developed within calc-silicate host rocks along the western margin of the batholith (red open circles) and xenoliths and/or screens (black dots). Contours in B reflect maxima for host rock structures only, not xenoliths and/or screens (i.e., red open circles); 1% area contours, contour interval = 2.0%/1% area.**

ous host rock. Screens represent kilometer-scale xenoliths that may be attached to the host rocks in the third dimension. Xenoliths and screens were mapped at scales ranging from 1:50,000 to 1:300 (i.e., outcrop scale) and comprise lithologies that are similar to the surrounding host rocks, including in decreasing abundance, calc-silicate rocks, marble, calcareous schist, calcareous conglomerate, psammitic schists and gneisses, migmatitic schist, serpentinized dunite and/or ultramafic rocks (Fig. 9; see also Nordgulen et al., 1992). Screens and associated xenolith swarms are generally clustered by rock type and are found within north-south–trending to arcuate swarms (Fig. 2). For example, marble bodies dominate the central portion of the batholith but are scarce to nonexistent westward. However, disparate lithologies of xenoliths commonly occur within xenolith swarms (e.g., Fig. 9F).

Calc-silicate xenoliths and screens are abundant in the western part of the batholith and likely correlate to the Sauren-Torghatten Nappe. Marble and ultramafic bodies are recognized within the interior of the pluton and probably correlate to the Lower or Middle Nappes. Xenoliths and screens of sillimanite-bearing quartzofeldspathic gneiss and pelitic migmatitic composition are dominantly found within the easternmost parts of the pluton, although pelitic xenoliths are scarce (Nordgulen et al., 1992). These rocks are correlated with the Upper Nappe based on lithologic and structural similarities. Despite the abundance and prevalence of xenoliths and screens that are indicative of the various Helgeland complex nappes, few xenoliths and/or screens of pelitic composition are found, even though pelitic rock types are represented within each nappe unit (e.g., Myrland, 1972).

The dimensions of xenoliths and screens within the Andalshatten batholith range from millimeters to 12 km long and range in area from square millimeters to almost 17 km$^2$. Xenolith and/or screen translation and rotation in the magma are recognized where the internal xenolith and/or screen structure (e.g., foliations, bedding) is discordant to equivalent structures in adjacent xenoliths and/or screens or host rocks. Xenoliths ranging in area from 100 to 0.001 m$^2$ are commonly found in more diverse orientations and mingle with xenoliths of different lithology (e.g., Figs. 9E, 9F). The orientations of mapped xenoliths and screens larger than 20 m$^2$ were determined by measuring the major axis of the rock body relative to north and are plotted in Figure 10A. Screens within the central and eastern parts of the batholith are elongate in the north-south direction; a significant population is oriented around N5°W (Fig. 10A). Screens within the western part of the batholith have long dimensions oriented parallel to the arcuate host rock contact (Fig. 2). Xenolith long axes are generally subparallel to the magmatic fabric in the batholith (Figs. 10A, 10B). Magmatic foliations exhibit little to no deflection around xenoliths and screens.

The contacts between host igneous rock and metamorphic xenoliths and/or screens are highly variable across all lithologies and display a range of concordant to discordant orientations with respect to internal structure (e.g., bedding, foliation). Figure 11 displays the complete range of contact types and orientations observed within the batholith. Contacts may be distinguished based on a range of cut-off angles between internal structures and the contact, where a 90° cut-off between internal planar structure (e.g., bedding, foliation) is discordant and a 0° cut-off is concordant (Fig. 11F). Contact-bedding cut-offs ranging from 0° to >50° occur along single, subplanar contacts (e.g., Fig. 11D). Sharp, highly discordant contacts are commonly found along kilometer-scale screens, but are also present at the edges of meter-scale bodies. Cuspate xenolith margins display centimeter- to meter-scale lobes of granodiorite that typically bow into the xenolith margin (e.g., Figs. 11D, 11E). Screens and xenoliths <100 m$^2$ tend to show internal ductile deformation, reactivation, and boudinage in the plane of the magmatic foliation that occurs in the host igneous rock. Restoration of ductilely deformed xenoliths provides a glimpse of the initial xenolith-magma geometry. Assuming two-dimensional plane strain, folded layers and the xenolith contact-magma cut-offs may be restored (Fig. 11F). This analysis indicates that the xenolith margins may have originated as jagged and planar contacts reminiscent of a dike contact.

Screens >0.5 km$^2$ display a variety of features that bear on the nature of magma emplacement. Contacts are generally discordant, planar, and stepped. Annotated photomosaic images of two screens are shown in Figures 12 and 13. Figure 12 illustrates a north-trending tabular screen (termed the "V" screen) that occurs in coarse-crystalline granodiorite (see Fig. 2 for location). Here, a vertical, west-northwest–facing cliff displays a tight antiform-synform pair, with an amplitude >90 m and wavelength ~20 m, developed in layered calc-silicate rocks (Figs. 12A, 12B). These folds are similar in morphology and orientation to those found in the southwestern aureole shown in Figure 8. The axial planes of the folds trend north-south. The screen is truncated along its top (east-facing side) by a jagged (1–3 m amplitude) intrusive contact, above which is an ~8-m-thick swarm of discoid-shaped mafic magmatic enclaves (Figs. 12B–12D; see also Fig. 6B). Similarly, Figure 13 illustrates the geometry and nature of a calc-silicate screen (termed the "Pirate's Galleon" screen) contained

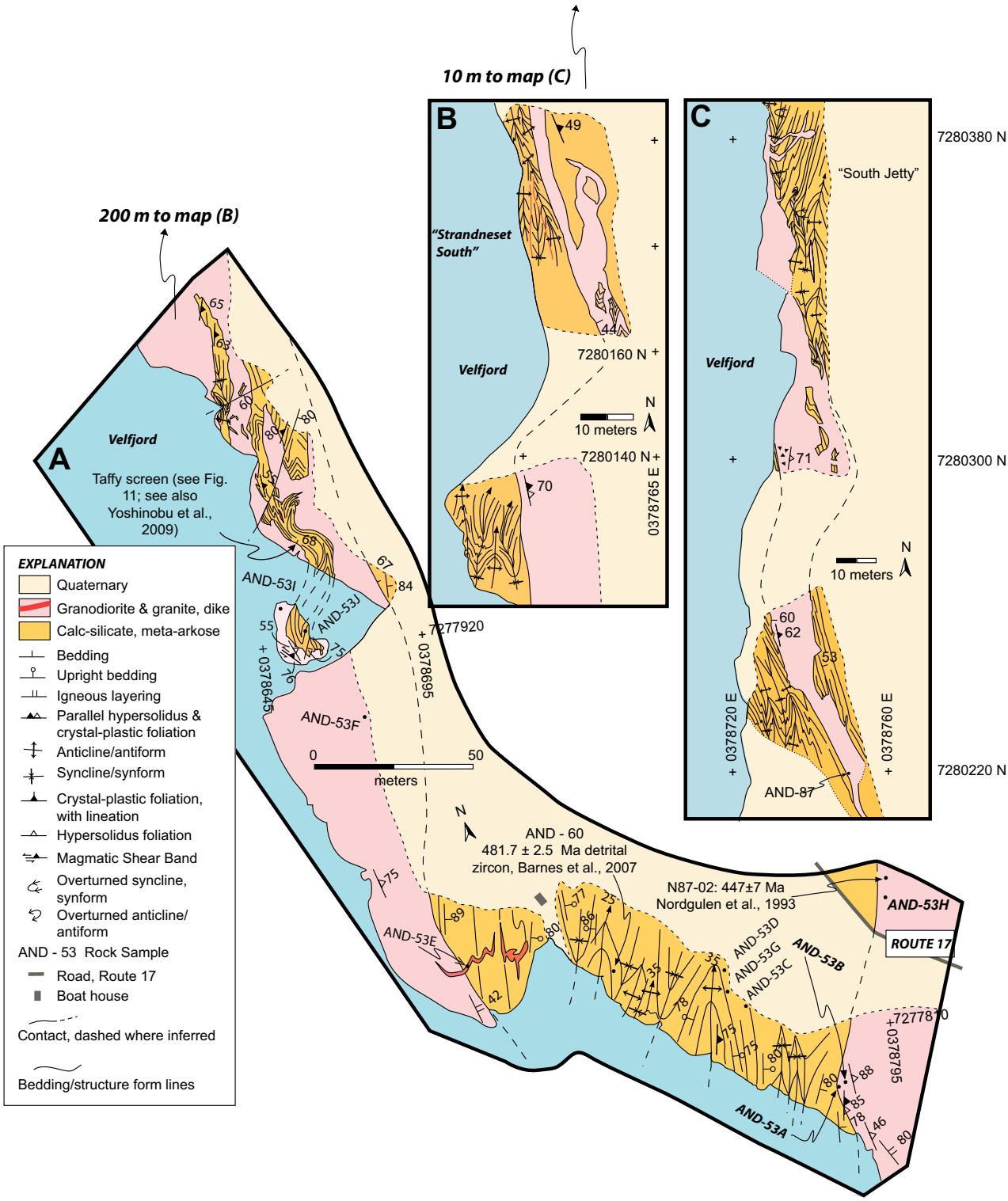


**Figure 8. Geologic grid maps of southwest contact aureole (see Fig. 2 for location) depicting emplacement-related reactivation and deformation of pre-emplacement, regional structures. Maps are shown at different scales. Geology in each map is spatially referenced to geodetic datum: WGS84, UTM Grid, Zone 33, base map Vevelstad 1:50,000, Kartblad 1826 III. (A) Southernmost grid map depicting structural relations in host rocks adjacent to western batholith contact. Note discordant and concordant contact relations between host rock structures and intrusive rocks. (B) Geologic grid map depicting preassembly folds reactivated by emplacement-related deformation. (C) Northernmost grid map depicting dike-like geometry of intrusive rocks and evidence for ductile and brittle deformation of host rocks during intrusion in the form of tightened fold interlimb angles and angular xenoliths. High-angle discordant host rock structure–intrusive contact cut-offs have been ductile deformed into shallower angles. Contacts between host rocks and dikes are curviplanar in orientation.**

within the diorite phase of the batholith. In map view, the Pirate's Galleon screen is ~300 m wide and tapers to ~30 m wide to the north (Fig. 2). In these exposures, an ~300-m-long discordant base of an internally folded calc-silicate screen is preserved along a steep, south-facing cliff (Figs. 13A, 13B). This relationship occurs along a west-trending ridge and can be observed from both the southern (Fig. 13B) and northern directions (Fig. 13C), providing a superb three-dimensional view of the base of a screen contained within the batholith. The base of the screen is intruded by diorite; upright, tight fold limbs are truncated along this contact. To the north, the same screen (Fig. 13C) is intruded by dikes near its base and calc-silicate xenoliths rotated within the host diorite while the diorite was partially molten. Based on the available exposure, it is not known whether such screens were attached to the host rocks in the third dimension. For example, the Pirate's Galleon screen may form a downward-projecting keel of metamorphic roof rock, akin to a stalactite in a cave.

## DISCUSSION

The relevant observational, structural, and geochronologic data sets described herein are summarized in schematic form in Figure 14. We discuss these data sets in the context of the following: (1) constraints on the duration and nature of magma emplacement as batches; (2) screen and xenolith incorporation and deformation during batholith assembly and the nature of the plutonic space problem; and (3) evidence for mobility of magma and incorporated host rock material within a paleo–magma chamber.

### Duration and Sequence of Assembly Based on Field Data and Geochronology

The current data are consistent with batholith assembly via early emplacement of porphyritic schlieren-banded to gneissic granodiorite, emplacement and sequential crystallization of porphyritic granodioritic magmas, and recharge by comagmatic dioritic magmas. Although zircon crystallization ages are not available for the schlieren-banded to gneissic granodiorite unit, these rocks are hypothesized to be early, but comagmatic with the main porphyritic granodiorite unit. Contacts between the porphyritic granodiorite unit and the schlieren-banded to gneissic granodiorite unit are sharp, implying that the porphyritic granodiorite is younger, and gradational, implying that the two were rheologically similar during emplacement and broadly synmagmatic. Furthermore, published major element data sets displaying smooth variations across the different units from northeast to south-

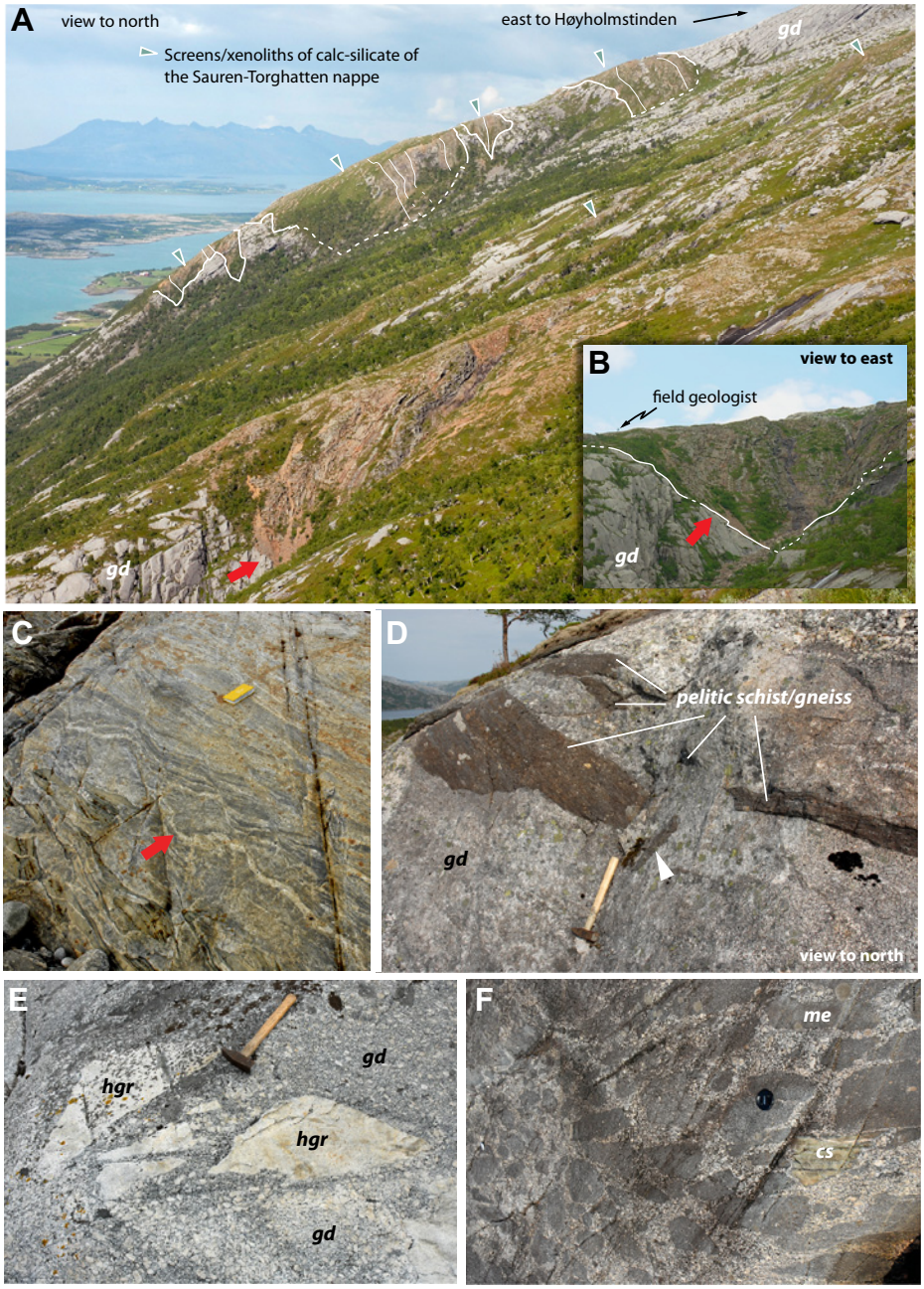


**Figure 9. Field photographs of xenoliths and screens in the Andalshatten batholith. (A) North view of calc-silicate screens in granodiorite (gd) along western margin of intrusion. Red arrow points to contact shown in B. (B) Base of screen is discordant to sedimentary layering and dips moderately east; geologist on ridge for scale. (C) Migmatitic argillaceous calc-silicate xenolith within granodiorite near western margin. Fish-shaped xenolith is surrounded by leucosome (red arrow). (D) Pelitic schist and gneiss xenoliths in various orientations in granodiorite of the central part of batholith. Note elongate microgranitoid enclave (white arrow). (E) Autoliths of hornblende granite (hgr) with angular margins contained within the megacrystic phase of the granodiorite. (F) Calc-silicate (cs) xenolith captured in swarm of microgranitoid enclaves (me) in megacrystic granodiorite.**

west (e.g., Nordgulen, 1993; Nordgulen et al., 1993) are consistent with the interpretation that the schlieren-banded to gneissic granodiorite observed along the eastern margin is related to the main porphyritic phase of the Andalshatten batholith. Therefore, the gneissic portions of this unit are most likely early batches of the (mostly?) solidified K-feldspar megacrystic porphyritic phase that were subsequently deformed during recharge of the growing batholith.

The new CA-TIMS ages indicate two distinct zircon crystallization ages and cooling intervals for the porphyritic granodioritic magmas that do not overlap in uncertainty. Crystallization of granodioritic magmas in the northwestern margin of the batholith occurred at 442.67 ± 0.14 Ma, whereas crystallization of zircons in the central region of the batholith, east of the swarm of large screens of calc-silicate rocks, occurred at 441.53 ± 0.40 Ma (Fig. 14). Given the uncertainties in the ages, crystallization of the two samples may have been separated by ~1 Ma. Detailed west-to-east mapping traverses did not identify internal contacts between these two chronologically distinct, but compositionally similar batches. However, the two samples are broadly separated by a number of kilometer-scale, discontinuous screens of metamorphic rocks (Figs. 2 and 14). The distribution of these screens in the context of the ages and batholith assembly is discussed in the following.

The new titanite ages are interpreted to reflect the closure temperature of titanite to Pb diffusion (e.g., Mattinson, 1978; Heaman and Parrish, 1991; Mezger et al., 1991, 1993; Spear and Parrish, 1996; Scott and St. Onge, 1995; Pidgeon et al., 1996; Frost et al., 2001), and thus provide preliminary constraints on the nature of cooling of the dated samples. The titanite dates of 441.30 ± 0.21 Ma (sample AND-12) and 436.1 ± 2.8 Ma (NAY-06–05) imply that the two granodioritic pulses of magma cooled through titanite closure (~650–700 °C, i.e., near the solidus) from margin to interior, and possibly at different rates (Fig. 15). We speculate that the variation in cooling rates reflects faster cooling in the northern portion of the batholith (sample AND-12) where, because of the triangular shape of the contact in map view, the surface area/volume ratio of the magma body is greater than the interior (sample NAY06–05; Fig. 14). However, additional geochronological studies should be conducted to define more precisely the crystallization and cooling history of the batholith.

Emplacement of dioritic magmas occurred in at least two distinct events while the porphyritic granodiorite was partially molten. Aligned swarms and conspicuous, dispersed microgranitoid enclaves indicate early dioritic input into the granodiorite followed by mingling and local mechanical mixing (e.g., Fig. 6). Subsequent injection of a voluminous batch of dioritic magmas into the central region of the batholith occurred while at least portions of the porphyritic granodiorite were above the solidus, as indicated by the presence of lobate-cuspate contacts and local pipe and flame structures of granodiorite that intruded overlying diorite (e.g., Fig. 6). It is plausible that the delayed titanite cooling in sample NAY06–05 (ca. 436.1 ± 2.8 Ma) may be the result of this heat addition in the central region of the batholith. However, the uncertainties in the titanite age for this sample are rather large.

## Screen and Xenolith Incorporation and Deformation

During assembly of the Andalshatten batholith, large coherent screens of marble, peridotite, and calc-silicate masses were isolated and incorporated by magma intrusion. These screens and xenolith swarms represent fragments of the Helgeland Nappe Complex and preserve relict host rock stratigraphy or ghost stratigraphy within the batholith (e.g., Pitcher, 1970). The largest screens (e.g., Figs. 12, 13, and 14) maintain lithologic continuity with the host rocks exposed along strike to the west and south, implying that these bodies were isolated relatively in situ by magma injection. The jagged and sharply discordant contacts of kilometer-scale screens (e.g., Figs. 12 and 13) are most consistent with formation by brittle failure via diking. These screens generally appear internally unaffected by incorporation into the magma, displaying no evidence for emplacement-related ductile deformation (e.g., synmagmatic boudinage, refolding, attenuation, bulbous contact relations). The hornblende biotite granite is only found cutting calc-silicate xenoliths and/or adjacent to the large screens; we speculate that this lithology may be the result of local anatexis of the more argillaceous horizons (e.g., Fig. 9C) within the calc-silicate screens and local migration of these leucocratic magmas as dikes into and along the calc-silicate screens.

The large swarm of kilometer-scale calc-silicate screens in the western region of the batholith defines an arcuate outcrop pattern that parallels the intrusive contact (Fig. 2). Individual screens have high axial ratios with the long axis subparallel to the intrusive contact. Internal planar structures within these screens mimic this arcuate trend over the outcrop area of the swarm. Together these observations are consistent with rigid rotation of the largest screens into subparallelism with the host rock contact during the addition of porphyritic granodioritic and dioritic magmas and westward expansion of the entire batholith. Rotation of some of the screens may have been ~30°–45° counterclockwise (in map view) in the southern portions of the batholith. Magmatic fabric trends define a similar arcuate orientation and may record emplacement-related, west-vergent flattening with or without shear within the crystallizing intrusion (cf. Grocott et al., 1999; Cruden, 2006) (Fig. 16). If this interpretation is correct, then a significant volume of the batholith was able to undergo viscous flow and deformation at conditions above the solidus in order to translate and rotate the large screens yet still preserve magmatic foliations.

In contrast, screens and xenoliths <~500 m long display evidence for synmagmatic inter-

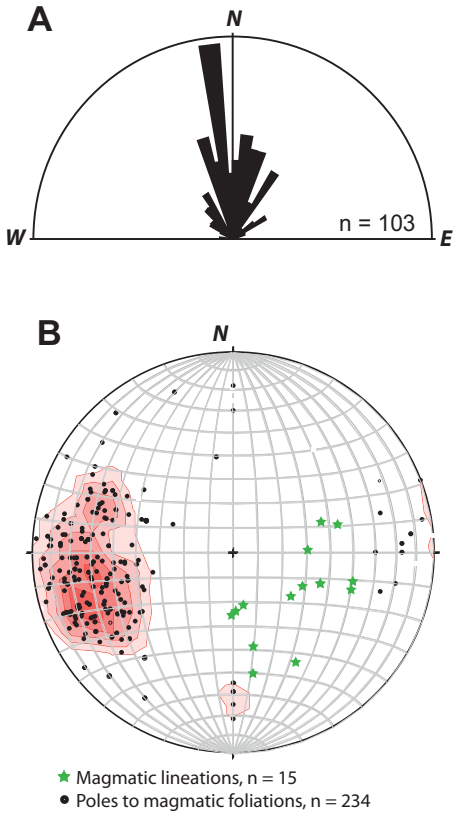


**Figure 10. Structural data for xenoliths and screens and fabrics within the Andalshatten batholith. (A) Rose diagram showing the orientations of elongate xenoliths and screens within the Andalshatten pluton that have areas >20 m². Xenoliths and screens have long axes that trend broadly north-south, with a population trending toward N5°W. (B) Lower hemisphere, equal-area stereonet displaying poles to magmatic foliations and magmatic lineations within the batholith.**

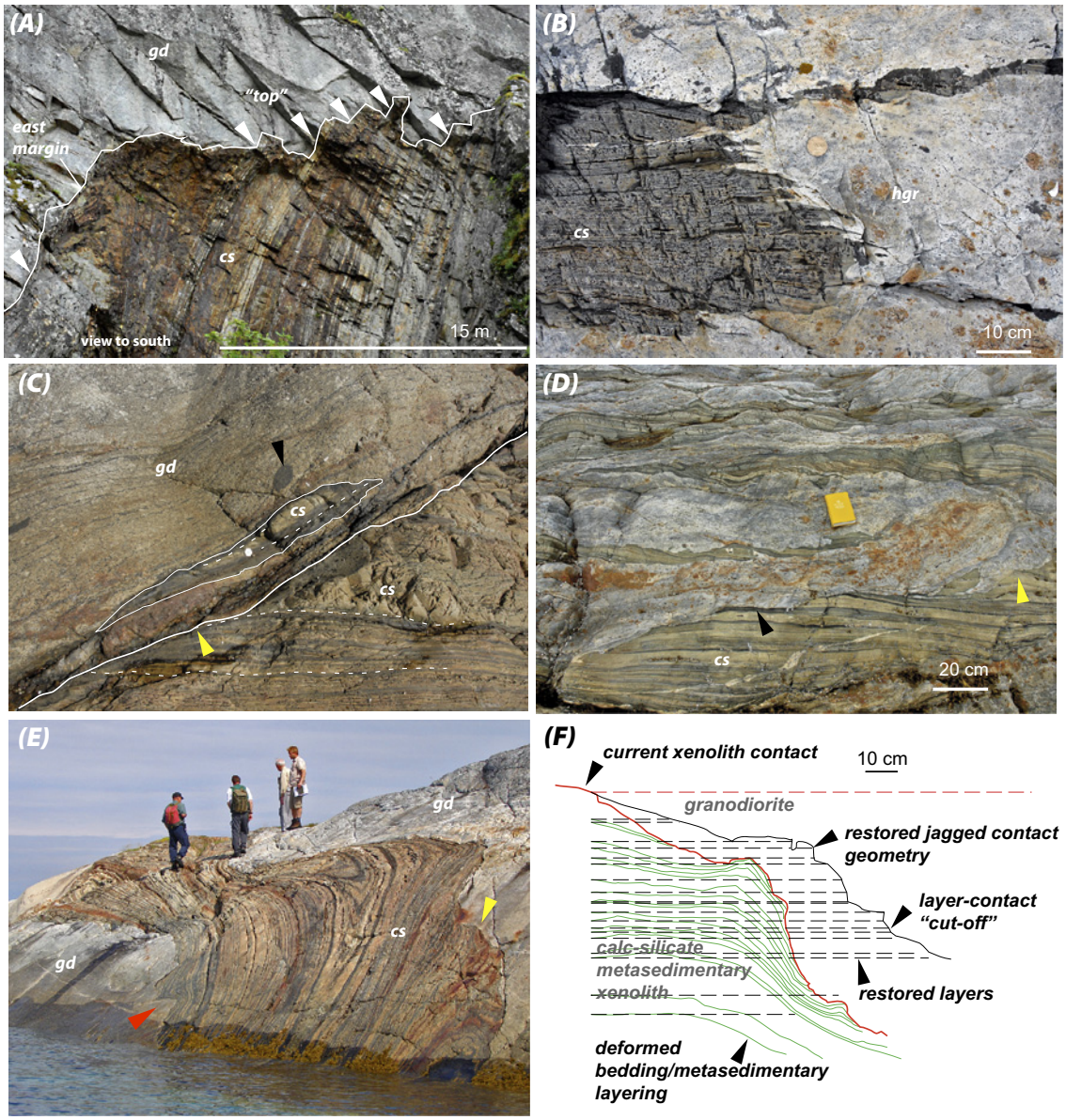


**Figure 11. Images of contact relations and internal deformation of xenoliths and screens. (A) East margin and top of a tabular calc-silicate (cs) screen in a vertical cliff face (gd—granodiorite). Note discordant margin and stepped upper intrusive contact. White arrows point to contacts parallel to internal bedding. (B) Centimeter-scale interfingering intrusive contact between calc-silicate xenolith and hornblende granite. (C) Rotated and/or translated calc-silicate xenolith subparallel to intrusive contact along western margin of batholith. Bedding (dashed white lines) within the calc-silicate rock is parallel to the long dimension of the image. Note elliptical microgranitoid enclave (black arrow). Coin in center of image is ~20 mm in diameter. (D) Attenuated, ductilely deformed calc-silicate xenoliths within hornblende granite. Contact-bedding cut-off angles (see text) vary from 0° (black arrow) to >50° (yellow arrow). (E) Ductilely deformed calc-silicate "taffy screen" in granodiorite, deformed like a piece of stretched taffy (see Fig. 8 for location). Note discordant intrusive cut-off between granodiorite and bedding (yellow arrow) and deflected bedding around protrusion of granodiorite into calc-silicate rock (red arrow; see Yoshinobu et al., 2009 for additional images). (F) Original and restored two-dimensional section (assuming plane strain) of a xenolith-granodiorite contact displaying initial jagged contact geometry that is subsequently ductilely deformed.**

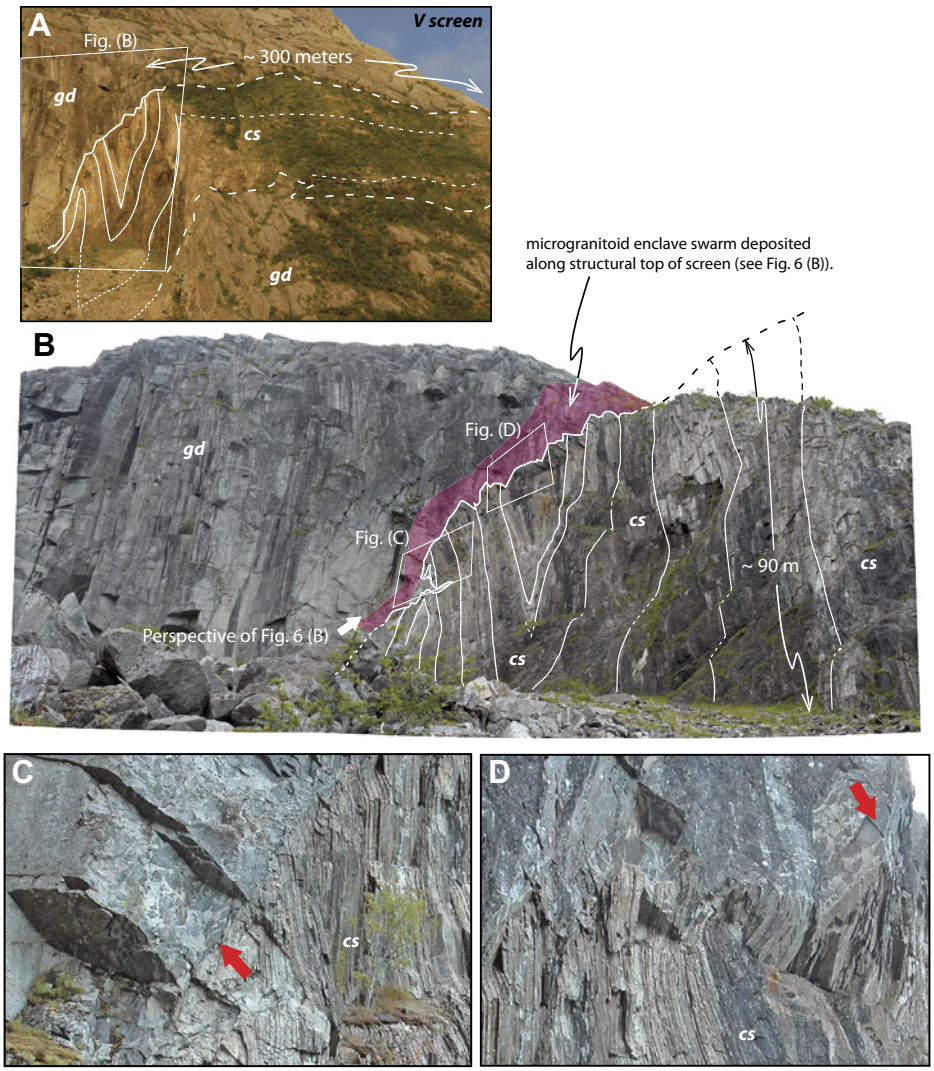


**Figure 12. The V screen (see Fig. 2 for location; see text for details). (A) Geological context of north-trending calc-silicate (cs) screen, ~500 m long and >100 m tall (gd—granodiorite). (B) Detailed photomosaic of upright, tight folds in the screen and the upper, jagged discordant contact. Semitransparent magenta zone illustrates a microgranitoid enclave swarm (depicted in Fig. 6B). (C, D) Telephoto images of the jagged contact and overlying disc-shaped microgranitoid enclaves (red arrows). Images were digitally colored enhanced to distinguish calc-silicate rocks and enclaves.**

nal deformation and diverse orientations with respect to the host rock reference frame. These smaller blocks commonly display internal structures that are discordant to the same structures in the adjacent host rocks and/or xenoliths. In some instances, translation and/or rotation of the xenolith restores the pre-emplacement host rock stratigraphy. However, where pervasive synmagmatic folding and/or boudinage or intermixing of xenoliths of differing rock type occurs (e.g., Fig. 9), host rock stratigraphy and/or structural continuity cannot be restored. Such synmagmatic strains and displacements of xenoliths are interpreted to indicate deformation of xenoliths while they were entrained in the magma (see also Yoshinobu et al., 2009).

## Tectonic Model for the Andalshatten Batholith

We use the phrase batholith tectonics to define the modes and nature of magma emplacement and assembly (i.e., building) of intrusions in the crust. A tectonic model for the Andalshatten batholith that invokes both multistage emplacement of magma into a growing crystal-laden reservoir (but not completely solidified?) as well as time-space variations in host rock rheology seems most consistent with the available data. Such a model should allow for some degree of mechanical and probably chemical interactions between sequentially crystallizing magmas above the solidus to explain the evidence for screen displacement and deformation within the voluminous granodiorite phase as well as both the concentration and dispersement of microgranitoid enclaves throughout the porphyritic granodiorite.

We envision a hybrid magmatic crack-seal cum metamorphic viscoelastic model of batholith tectonics for the Andalshatten intrusion (Fig. 17). This model is based on the concepts of incremental emplacement of magma batches (e.g., Richey, 1927; Lagarde et al., 1990; Glazner et al., 2004; Bartley et al., 2008, 2012; Miller et al., 2011) but takes into account the abundant evidence for both brittle and ductile deformation in the host rocks and xenoliths (cf. Rubin, 1993; Miller and Paterson, 1999), as well as magma and xenolith and/or screen mobility in the evolving and growing intrusion. The model may be tested with additional high-precision CA-TIMS analyses coupled with trace element microanalysis of accessory phases, hornblende, and feldspars to assess the magnitude of in situ versus in transit and source-related chemical effects (e.g., Schoene et al., 2010, 2012).

Assembly of the Andalshatten batholith initiated with the intrusion of north-trending tabular sheets of granodioritic and tonalitic magma into pelitic migmatites of the Upper Nappe (Fig. 17A). During magma intrusion, kilometer-scale screens of calc-silicate gneiss, marble, and minor pelitic migmatite were stranded between successive sheets and incorporated into the growing batholith. The earliest granodioritic magmas formed the northeastern apophasis (Figs. 4 and 17A). Continued emplacement of porphyritic granodiorite to the west as kilometer-scale north-trending elongate batches occurred across the Sauren-Torghatten and Upper Nappe framework, forming the eventual central and western regions of the batholith (Fig. 17A). Zircon in the northwesternmost body crystallized ca. 442 Ma and titanite in the same sample cooled through its closure temperature to Pb loss ~1 Ma later. During or soon after zircon crystallization ca. 442 Ma, porphyritic granodioritic magmas were emplaced to the east of these magmas (Fig. 17B). These contemporaneous or younger magmas crystallized zircon ca. 441 Ma. Discontinuous screens of calc-silicate metamorphic rocks separated the two zones of magma accumulation but did not impede hypersolidus interaction between the two regions in the form of recharge of the porphyritic granodiorite by

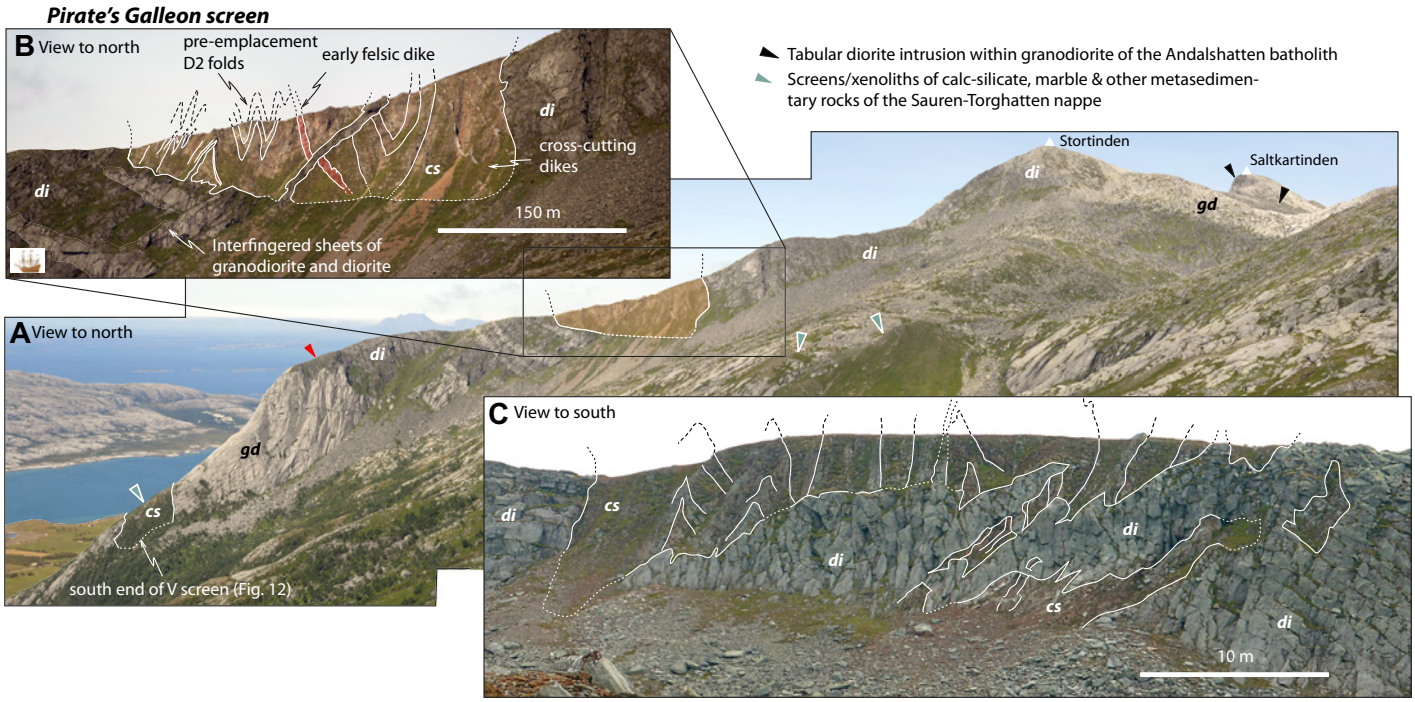


**Figure 13. The Pirate's Galleon screen (see Fig. 2 for location). (A) Photomosaic of the south side of Stortinden ridge showing location of the "Pirate screen" (see text) (decorated with orange) within diorite. Diorite crops out as tabular to bulbous intrusions within the granodiorite (cf. with Fig. 4D). Note variable east-dipping basal contact (red triangle) of diorite (di) above granodiorite (gd). Calc-silicate (cs) xenoliths and screens are also preserved within the granodiorite (green arrows). (B) Detailed view of the Pirate screen looking north, displaying preexisting folds truncated along structural base of the screen. (C) View to the south of the northern tip of the Pirate screen displaying discordant base and xenoliths of calc-silicate in various orientations in the host diorite.**

dioritic magmas, mechanical mingling of the two (e.g., Fig. 6), and diachronous magmatic foliation formation. Westward expansion of the batholith by the input of additional granodioritic magma into the central region continued and included voluminous dioritic magmas during and/or soon after zircon crystallization ca. 441 Ma, but prior to reaching the porphyritic granodiorite solidus. Calc-silicate lithologies and lesser amounts of calcareous conglomerate of the Sauren-Torghatten Nappe were the principal rock types entrained during this stage of emplacement (Fig. 17C).

Recharge of the porphyritic granodiorite in the central region by intrusion of the diorite produced (1) the conspicuous microgranitoid enclave swarms aligned within the magmatic foliation and along the eastern (upper) contact of the V screen (e.g., Figs. 6B and 12), (2) nested mafic-felsic sills in the structurally higher regions of exposure (Fig. 4D), and (3) additional heat and mass to stall cooling of the batholith. As the dioritic magmas were emplaced as sheets into the growing intrusion (e.g., Figs. 4C and 17C), eastward tilting of the western portions of the intrusion occurred about a subhorizontal axis. This resulted in the steepening of contacts between mafic and felsic intrusions (e.g., Fig. 6A), magmatic foliations, and the overall eastern dip of the western batholith–host rock contact. Continued upward and outward (i.e., to the west) emplacement of granodioritic and dioritic magmas contributed to this west-directed inflation of the batholith (Fig. 17C).

Multiple space-making processes were operative during the assembly of the Andalshatten batholith. The numerous mapped dikes of granodiorite (e.g., Fig. 8) along the western margin as well as the regional discordance of the batholith with respect to the north-trending nappes within the Helgeland Nappe Complex (e.g., Fig. 1) indicate that the host rocks periodically deformed by brittle failure during magma emplacement. However, elongate screens and xenoliths, presumably formed by propagation of pressurized magmatic sheets and cracking of the host rocks during earlier episodes of magma emplacement, were involved in viscous deformation near the margins of the magma chamber as well as translation and/or rotation during subsequent magma emplacement and the turgid growth of the batholith. Depression of the floor of the batholith occurred during the influx of later magma pulses such as the diorite. The deformation mechanism that facilitated floor downdrop adjacent to the growing intrusion was likely viscous flow including high-temperature creep, as observed in the western contact aureole (cf. Cruden and McCaffrey, 2001; Dumond et al., 2005). Roof exposures were eroded away and so it is not possible to place constraints on the complete three-dimensional displacement field attending batholith assembly. However, we suggest that mechanisms such as roof uplift as envisioned for laccoliths are inconsequential at lithostatic loads appropriate for the middle crust (e.g., Cruden, 2006). Given the evidence for magma-up, host rock–down displacement along both the vertical eastern margin and arcuate, steep to east-dipping western margin, we suggest that one vector of host rock displacement was down and outward, yielding a quasi-lopolith shape to the batholith in cross section (Figs. 3, 14, and 17; Fig. 2 in Grout, 1918).

Compared to other mapped intrusions of equivalent size in the Bindal Batholith (e.g., Gustavson, 1981) as well as other terranes (e.g., Bateman, 1992), the Andalshatten is rich in its spatial extent (8% of batholith area) and diversity of metamorphic screens and xenoliths. In the Cretaceous Sierra Nevada batholith, California, Saleeby (1990) noted how the

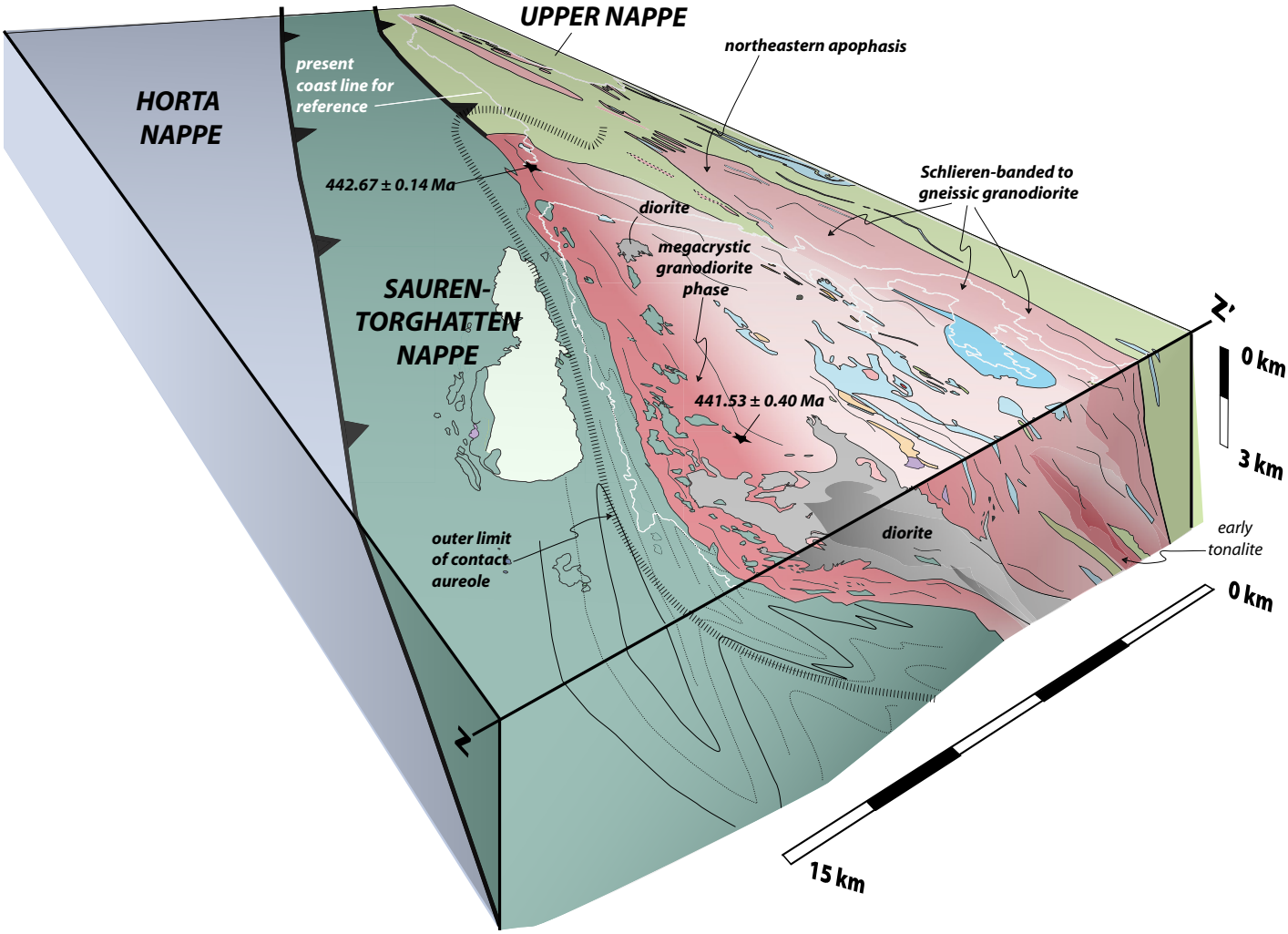


**Figure 14. Oblique perspective of the Andalshatten batholith based on available geological data. Location of z–z′ is from Figure 2. Screens in the central and eastern portions of the batholith maintain the colors of Figure 2. To highlight geometry and distribution of ghost stratigraphy, the calc-silicate host rocks of the Sauren-Torghatten Nappe and equivalent calc-silicate screens in the western part of the batholith are shown in dark green (as in Fig. 1).**

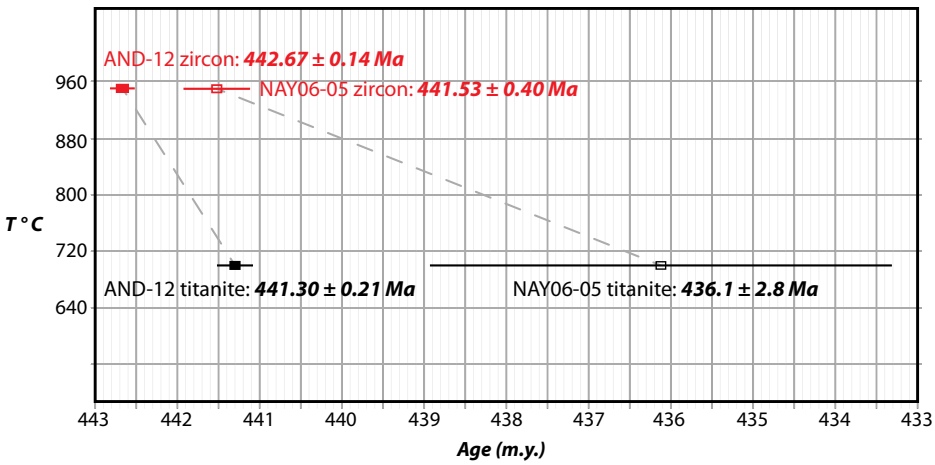


**Figure 15. Cooling history for porphyritic granodiorite unit. Filled rectangle is sample AND-12 (northern apex of batholith, Fig. 2); open rectangle is sample NAY06–05 (central portion of batholith, Fig. 2). Age uncertainties are illustrated with bold lines. Zircon and titanite closure temperatures (*T*) to Pb loss are chosen to be 950 °C and 700 °C, respectively (Cherniak and Watson, 2001; Scott and St. Onge, 1995).**

metamorphic framework rocks that host the various plutons were preserved within and between plutons with zircon ages between ca. 115 and 85 Ma. (Fig. 1 in Saleeby, 1990; cf. Fig. 7 in Dickinson, 2008). Such interpluton wall rock screens have been variously interpreted as forming by megastoping (e.g., Bartley and Glazner, 1998) and/or crustal-scale return flow (e.g., Tobisch et al., 1986; Saleeby, 1990). Regardless, the Sierran examples of interpluton screens represent the intrusive boundaries between distinct, mappable igneous phases with diverse crystallization ages and petrologic histories. We hypothesize that the intrabatholith screens within the Andalshatten intrusion may reflect a similar history of sequential magma emplacement and host rock displacement, but over a significantly shorter duration, i.e., the temporal scale of emplacement of all of the magma batches that eventually coalesced to form the Andalshatten batholith. As such, the broad trend of screens and xenolith swarms may grossly reflect the discontinuously preserved boundaries of former elongate magma batches. Likewise, the width of preserved intrusive rock between screens represents the approximate maximum width of individual magma batches. It is plausible that even smaller magma batches may have coalesced to form the expansive regions of granodiorite between screens. However, no evidence of these smaller batches has been observed.

According to our interpretation, the screens within the western margin are arcuate, owing in part to their outward rotation during subsequent magma injection. Therefore, disruption of the batches and their ephemeral contacts may be due partly to continued emplacement of magma within the growing chamber. Given the negative buoyancy of calc-silicate and other metamorphic rock types in granodioritic magmas, the preservation of the large screens and xenoliths implies that the magmas of the Andalshatten batholith had sufficient yield strength to suspend the largest blocks. We hypothesize that the large screens are held floating in their position because of the increase in magma strength due to crystallization driven by cooling adjacent to the largest screens. Thus, it seems likely that the swath of calc-silicate screens in the western exposures of the batholith reflects a disrupted paleo–contact zone between two batches of partially molten granodioritic magma.

The fact that screens are discontinuous in outcrop from the southern to northern contact and porphyritic granodiorite occurs on either side of the screens (e.g., Figs. 2 and 3) has two interesting implications. First, some proportion of the preintrusive metamorphic rocks now occupied by the batholith has been removed from the map plane; otherwise it should be possible to reconstruct the host rock tectonostratigraphy by removing the mapped intrusion and restoring the host rock tectonostratigraphy (e.g., Marko and Yoshinobu, 2011). Second, if our interpretation of the screens as both the incomplete remnant boundaries of individual batches as well as rigid passive markers that record displacement in a magma is correct, then it is plausible that the boundaries that existed between adjacent batches were porous and allowed mechanical and chemical interactions to occur between batches. Therefore, the partially molten portions of the Andalshatten batholith may have been aerially extensive, i.e., on the scale of the outcrop extent of the porphyritic granodiorite phase.

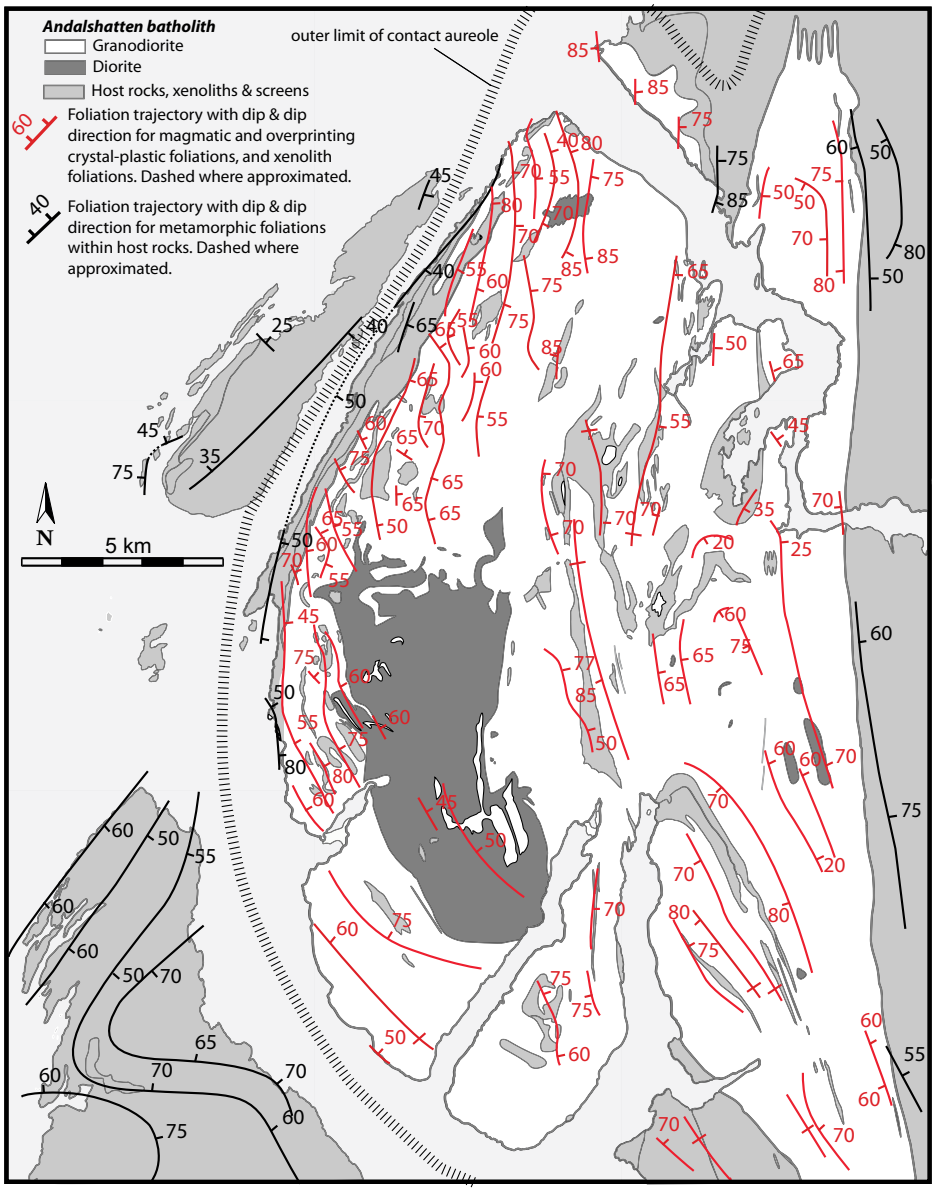


**Figure 16. Form line map of magmatic and metamorphic foliations in the Andalshatten batholith based on strike and dip data in Figure 2.**

## SUMMARY AND CONCLUSIONS

We interpret the Andalshatten batholith to have been assembled via multistage emplacement of tonalite, granodiorite, and diorite magma batches that intruded across the north-trending Helgeland Nappe Complex in the middle crust of an Ordovician arc. At present, the distinction of magma batches can only be made based on the mapped lithologic and tex-

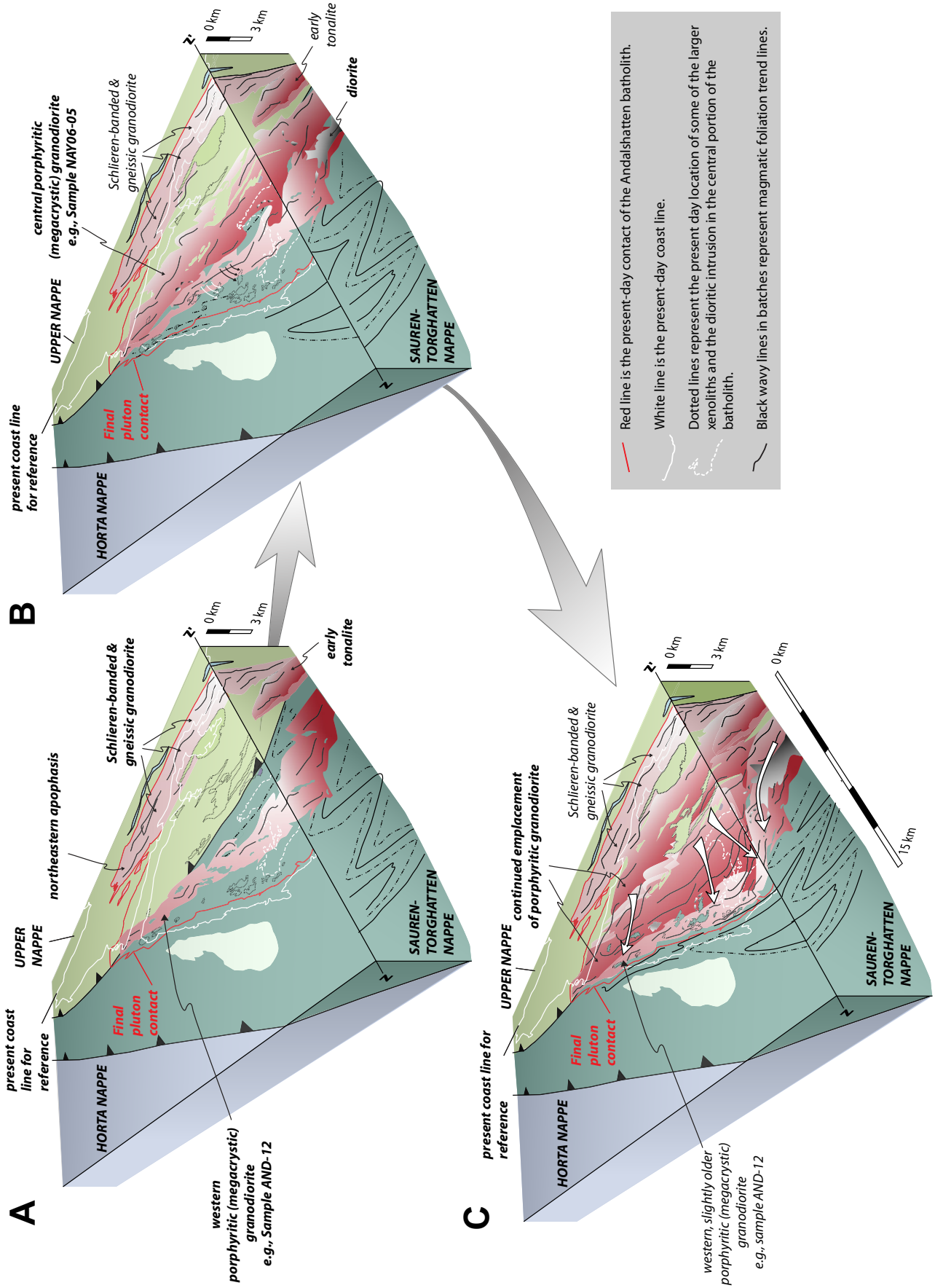


**Figure 17. Speculative sequential evolution of the assembly of the Andalshatten batholith based on available U-Pb geochronology and field relations; colors as in Figure 2. (A) Pre–442 Ma configuration of the Helgeland Nappe Complex. (B) Early emplacement of tonalite and eastern phases of schlieren-banded granodiorite, megacrystic granodiorite, and gneissic granodiorite. (C) Continued emplacement of granodiorite and megacrystic granodiorite as currently exposed along western half of mapped batholith.**

tural variations described herein. Based on the uncertainties in zircon crystallization from the CA-TIMS analyses, the minimum duration of zircon crystallization is ~1 Ma for the porphyritic granodiorite unit exposed in the northwest and central regions of the batholith. Field relations and published major element and isotopic data support the notion that all of the major compositional units within the 322 km$^2$ batholith were comagmatic. However, it is unknown whether the entire mapped batholith was above the solidus for some duration of crystallization and magma emplacement at the same time. Additional high-precision U-Pb ages obtained for samples from the eastern regions of the batholith coupled with trace element and isotopic analyses of accessory phases are required to evaluate the absolute duration of zircon crystallization in the entire batholith and the extent or existence of in situ differentiation across various lithologies.

We envision hypersolidus regions within the growing magma chamber to be spatially and temporally transient, reflecting the local rate and duration of recharge into the reservoir. Periodic or continuous input of new magma in different regions of the magma chamber added heat and mass, allowing ambient near-solidus or hypersolidus temperatures to be maintained. We suggest that the partially molten regions of the Andalshatten magma chamber were at least as large as, if not larger than, the width of the granodiorite that currently crops out between the western contact and the extensive swarm of calc-silicate screens.

Local space for batholith assembly was accommodated by brittle deformation (i.e., diking, stoping) and viscous flow of host rocks in a dynamothermal contact aureole. Viscous flow was facilitated by reactivation of existing structures, penetrative foliation development, and lateral and downward-directed displacement of host rocks along the western margin during batholith expansion and growth. Kilometer-scale screens were incorporated during emplacement of magma batches and form a ghost stratigraphy that preserves the gross host rock framework prior to batholith emplacement. These screens were internally rigid but rotated and translated into an arcuate orientation during subsequent magma emplacement into the turgid batholith. In contrast, subkilometer xenoliths were deformed viscously at hypersolidus conditions during subsequent growth of the turgid batholith. The scale dependence of synmagmatic deformation of screens and xenoliths is likely the result of smaller blocks becoming thermally equilibrated with the surrounding magma and thus deforming by ductile mechanisms. Given the lack of penetrative solid-state deformation and the widespread presence of magmatic foliations, it is plausible that a magma chamber of significant volume existed and was capable of undergoing mechanical and chemical changes at hypersolidus conditions during batholith assembly.

## ACKNOWLEDGMENTS

Funded by National Science Foundation grant 0439750 and a grant from the Geological Society of America. The Norwegian Geological Survey, the Department of Geosciences, and the College of Arts and Sciences at Texas Tech University are gratefully acknowledged for their continued support of our research in Norway. Arnt Mathias Arntzen provided exquisite food, shelter, and conversation at Handelsstedet Forvik AS during our time in the field. Cal Barnes, Carol Frost, Keegan Schmidt, and Ron Vernon provided detailed and instructive comments prior to submittal, and we warmly acknowledge their insights as well as their commitment to helping improve the clarity of our writing. *Geosphere* editors Carol Frost and Mike Williams provided exceptionally detailed guidance during revisions of the manuscript, and Calvin Miller and an anonymous reviewer provided detailed reviews that helped to strengthen and clarify this work.

We warmly acknowledge Bernard Bonin for the opportunity to showcase the Andalshatten batholith during the Eurogranites 2011 Field Conference and all of the conference participants for their insightful questions and comments. We thank Cal Barnes, Olivier Bachmann, John Bartley, Sandy Cruden, Allen Glazner, Vali Memeti, Calvin Miller, Bob Miller, and Scott Paterson for ongoing, fruitful electronic and verbal discussions regarding magmatic systems. The stereonets were made with OS-Stereonet developed by Netor Cardozo and Rick Allmendinger (http://download.cnet.com/OSXStereonet/3000-2054_4-75532277.html). Yoshinobu gratefully acknowledges Roel Verberne, David Floess, and Othmar Muntener for their invitation to spend time at the University of Lausanne discussing magma emplacement processes as well as suggesting the concept of batholith tectonics.

## REFERENCES CITED

Ague, J.J., and Brimhall, G.H., 1988, Regional variations in bulk chemistry, mineralogy, and the compositions of mafic and accessory minerals in the batholiths of California: Geological Society of America Bulletin, v. 100, p. 891–911, doi:10.1130/0016-7606(1988)100<0891:RVIBCM>2.3.CO;2.

Anderson, H., Yoshinobu, A., and Barnes, C.G., 2005, Deformation, migmatization, and intrusive diatexites along the contact of the ~470 Ma Vega pluton, Helgeland Nappe Complex, north-central Norway: Eos (Transactions, American Geophysical Union), Fall Meeting Supplement, abs. V13E–0597.

Balk, R., 1937, Structural behavior of igneous rocks: Geological Society of America Memoir 5, 177 p.

Barnes, C.G., and Prestvik, T., 2000, Conditions of pluton emplacement and anatexis in the Caledonian Bindal Batholith, north-central Norway: Norsk Geologisk Tidsskrift, v. 80, p. 259–274, doi:10.1080/00291960051030581.

Barnes, C.G., Frost, C.D., McArthur, K., Barnes, M.A., Allen, C.M., Nordgulen, Ø., Prestvik, T., and Yoshinobu, A.S., 2007, Timing of sedimentation, metamorphism, and plutonism in the Helgeland Nappe Complex, north-central Norwegian Caledonides: Geosphere, v. 3, p. 683–703, doi:10.1130/GES00138.1.

Barnes, C.G., Reid, K., Frost, C.D., Barnes, M.A., Allen, C.M., and Yoshinobu, A.S., 2011, Ordovician and Silurian magmatism in the Upper Nappe, Uppermost Allochthon, Helgeland Nappe Complex, north-central Norway: Norwegian Journal of Geology, v. 91, p. 121–136.

Bartley, J.M. and Glazner, A.F., 1998, Megastoping and the formation of interpluton wall rock screens in the Sierra Nevada, California: Geological Society of America Abstracts with Programs, v. 30, no. 5, p. 4.

Bartley, J.M., Coleman, D.S., and Glazner, A.F., 2008, Incremental pluton emplacement by magmatic crack-seal: Royal Society of Edinburgh Transactions, Earth Sciences, v. 97, p. 383–396, doi:10.1017/S0263593300001528.

Bartley, J.M., Glazner, A.F., and Mahan, K.H., 2012, Formation of pluton roofs, floors, and walls by crack opening at Split Mountain, Sierra Nevada, CA: Geosphere, v. 8, p. 1086–1103, doi:10.1130/GES00722.1.

Bateman, P.C., 1992, Plutonism in the central part of the Sierra Nevada batholith, California: U.S. Geological Survey Professional Paper 1483, 186 p.

Birkeland, A., Nordgulen, O., Cumming, G.L., and Bjorlkke, A., 1993, Pb-Nd-Sr isotopic constraints on the origin of the Caledonian Bindal batholith, central Norway: Lithos, v. 29, p. 257–271, doi:10.1016/0024-4937(93)90020-D.

Chen, J.H., and Moore, J.G., 1982, Uranium-lead isotopic ages from the Sierra Nevada batholith, California: Journal of Geophysical Research, v. 87, p. 4761–4784, doi:10.1029/JB087iB06p04761.

Cherniak, D.J., and Watson, E.B., 2001, Pb diffusion in zircon: Chemical Geology, v. 172, p. 5–24, doi:10.1016/S0009-2541(00)00233-3.

Ciavarella, V., and Wyld, S.J., 2008 Wall rocks as recorders of multiple pluton emplacement mechanisms—Examples from Cretaceous intrusions of northwest Nevada, *in* Wright, J.E., and Shervais, J.W., eds., Ophiolites, arcs, and batholiths: A tribute to Cliff Hopson: Geological Society of America Special Paper 438, p. 517–550, doi:10.1130/2008.2438(19).

Clarke, B.D., and Erdmann, S., 2008, Is stoping a volumetrically significant pluton emplacement process?: Geological Society of America Bulletin, v. 120, p. 1072–1074, doi:10.1130/B26147.1.

Coleman, D.S., Gray, W., and Glazner, A.F., 2004, Rethinking the emplacement and evolution of zoned plutons: Geochronologic evidence for incremental assembly of the Tuolumne Intrusive Suite, California: Geology, v. 32, p. 433–436, doi:10.1130/G20220.1.

Cruden, A.R., 2006, Emplacement and growth of plutons: Implications for rates of melting and mass transfer in continental crust, *in* Brown, M., and Rushmer, T., eds., Evolution and differentiation of the continental crust: Cambridge, Cambridge University Press, p. 454–519.

Cruden, A.R., and McCaffrey, K.J.W., 2001, Growth of plutons by floor subsidence: Implications for rates of emplacement, intrusion spacing and melt-extraction mechanisms: Physics and Chemistry of the Earth. Part A: Solid Earth and Geodesy, v. 26, p. 303–315, doi:10.1016/S1464-1895(01)00060-6.

Daly, R.A., 1903a, The mechanisms of igneous intrusion: American Journal of Science, v. 15, p. 269–298, doi:10.2475/ajs.s4-15.88.269.

Daly, R.A., 1903b, The mechanisms of igneous intrusion: American Journal of Science, v. 16, p. 107–126, doi:10.2475/ajs.s4-16.92.107.

de Saint-Blanquat, M., Habert, G., Horsman, E., Morgan, S.S., Tikoff, B., Launeau, P., and Gleizes, G., 2006, Mechanisms and duration of non-tectonically assisted magma emplacement in the upper crust: The Black Mesa pluton, Henry Mountains, Utah: Tectonophysics, v. 428, p. 1–31, doi:10.1016/j.tecto.2006.07.014.

Dickinson, W.R., 2008, Accretionary Mesozoic–Cenozoic expansion of the Cordilleran continental margin in California and adjacent Oregon: Geosphere, v. 4, p. 329–353, doi:10.1130/GES00105.1.

Didier, J., and Barbarin, B., eds., 1991, Enclaves and granite petrology: Developments in Petrology, Volume 13: Elsevier, Amsterdam, 625 p.

Dumond, G., Yoshinobu, A., and Barnes, C.G., 2005, Mid-crustal emplacement of the Sausfjellet pluton, central Norway: Ductile flow, stoping and in situ assimilation: Geological Society of America Bulletin, v. 117, p. 383–395, doi:10.1130/B25464.1.

Frost, B.R., Chamberlain, K.R., and Schumacher, J.C., 2001, Sphene (titanite): Phase relations and role as a geochronometer: Chemical Geology, v. 172, p. 131–148, doi:10.1016/S0009-2541(00)00240-0.

Gilluly, J., 1948, Origin of granite: Geological Society of America Memoir 28, 139 p.

Glazner, A.F., and Bartley, J.M., 2006, Is stoping a volumetrically important pluton emplacement process?: Geological Society of America Bulletin, v. 118, p. 1185–1195, doi:10.1130/B25738.1.

Glazner, A.F., and Bartley, J.M., 2008, Reply to comments on "Is stoping a volumetrically important pluton emplacement process?": Geological Society of America Bulletin, v. 120, p. 1082–1087.

Glazner, A.F., Bartley, J.M., Coleman, D.S., Gray, W., and Taylor, R.Z., 2004, Are plutons assembled over millions of years by amalgamation from small magma chambers?: GSA Today, v. 14, no. 4–5, p. 4–11, doi:10.1130/1052-5173(2004)014<0004:APAOMO>2.0.CO;2.

Glazner, A.F., Bartley, J.M., and Coleman, D.S., 2010, The room non-problem: Paper 10-6: Geological Society of America Abstracts with Programs, v. 42, no. 4, p. 52.

Grocott, J., Garde, A., Chadwick, B., Cruden, A.R., and Swager, C., 1999, Emplacement of rapakivi granite and syenite by floor depression and roof uplift in the Palaeoproterozoic Ketilidian orogen, south Greenland: Geological Society of London Journal, v. 156, p. 15–24, doi:10.1144/gsjgs.156.1.0015.

Grout, F.F., 1918, The lopolith; an igneous form exemplified by the Duluth gabbro: American Journal of Science, v. 46, p. 516–522, doi:10.2475/ajs.s4-46.273.516.

Gustavson, M., 1978, Caledonides of north-central Norway, *in* Caledonian-Appalachian orogen of the North Atlantic region: Geological Survey of Canada Paper 78-13, p. 25–30.

Gustavson, M., 1981, Mosjoen: Norges Geologiske Undersøkelse, scale 1:25,000.

Hanson, R.B., and Glazner, A.F., 1995, Thermal requirements for extensional emplacement of granitoids: Geology, v. 23, p. 213–216, doi:10.1130/0091-7613(1995)023<0213:TRFEEO>2.3.CO;2.

Hardee, H.C., 1982, Incipient magma chamber formation as a result of repetitive intrusions: Bulletin of Volcanology, v. 45, p. 41–49, doi:10.1007/BF02600388.

Heaman, L.M., and Parrish, R., 1991, U-Pb geochronology of accessory minerals, *in* Heaman, L.M., and Ludden, J.N., eds., Applications of radiogenic isotope systems to problems in geology: Mineralogical Association of Canada Short Course 19, p. 59–102.

Heldal, T., 1987, Stratigrafi og strukurell utvikling I Saurenomradet, vest for Bronnoysund, sydlige Nordland [thesis]: Bergen, Norway, University of Bergen, 293 p.

Heldal, T., 2001, Ordovician stratigraphy in the western Helgeland Nappe Complex in the Bronnoysund area, north-central Norway: Norges Geologiske Undersøkelse Bulletin, v. 438, p. 47–61.

Heldal, T. and Hjelmeland, H., 1988, Bronnoysund, berggrunnskart 1725–1, forelopig, utgave: Norges Geologiske Undersøkelse, scale 1:50,000.

Huber, C., Bachmann, O., and Dufek, J., 2011, Thermo-mechanical reactivation of locked crystal mushes: Melting-induced internal fracturing and assimilation processes in magmas: Earth and Planetary Science Letters, v. 304, p. 443–454, doi:10.1016/j.epsl.2011.02.022.

Hutton, D.H.W., 1996, The "space problem" in the emplacement of granite: Episodes, v. 19, p. 114–119.

Jaffey, A.H., Flynn, K.F., Glendenin, L.E., Bentley, W.C., and Essling, A.M., 1971, Precision measurements of half-lives and specific activities of $^{235}$U and $^{238}$U: Physical Review C: Nuclear Physics, v. 4, p. 1889–1906, doi:10.1103/PhysRevC.4.1889.

Kollung, S., 1967, Geologiske undersokelser I der sorlige Helgeland of nordlige Namdal: Norges Geologiske Undersøkelse Bulletin, v. 254, p. 1–95.

Krauskopf, K.B., 1968, A tale of ten plutons: Geological Society of America Bulletin, v. 79, p. 1–18, doi:10.1130/0016-7606(1968)79[1:ATOTP]2.0.CO;2.

Krogh, T.E., 1973, A low-contamination method for hydrothermal decomposition of zircon and extraction of U and Pb for isotopic age determinations: Geochimica et Cosmochimica Acta, v. 37, p. 485–494, doi:10.1016/0016-7037(73)90213-5.

Lagarde, J.L., Brun, J.P., and Gapais, D., 1990, Formation of epizonal granitic plutons by in situ assemblage of laterally expanding magma: Paris, Academie des Sciences Comptes Rendus, v. 310, ser. II, p. 1109–1114.

Ludwig, K.R., 1980, Calculation of uncertainties of U-Pb isotope data: Earth and Planetary Science Letters, v. 46, p. 212–220, doi:10.1016/0012-821X(80)90007-2.

Ludwig, K.R., 1988, PBDAT for MS-DOS, a computer program for IBM-PC compatibles for processing raw Pb-U-Th isotope data, version 1.24: U.S. Geological Survey Open-File Report 88–542.

Ludwig, K.R., 1991, ISOPLOT for MS-DOS, a plotting and regression program for radiogenic-isotope data, for IBM-PC compatible computers, version 2.75: U.S. Geological Survey Open-File Report 91–445.

Ludwig, K.R., 1998, On the treatment of concordant uranium-lead ages: Geochimica et Cosmochimica Acta, v. 62, p. 665–676, doi:10.1016/S0016-7037(98)00059-3.

Ludwig, K.R., 2000, Decay constant errors in U-Pb concordia-intercept ages: Journal of Chemical Geology, v. 166, p. 315–318, doi:10.1016/S0009-2541(99)00219-3.

Marko, W.T., 2012, The petrology, emplacement history, and tectonic setting of the Vega intrusive complex, southern Nordland, Norway [Ph.D. thesis]: Lubbock, Texas Tech University, 305 p.

Marko, W.T., and Yoshinobu, A.S., 2011, Using restored cross sections to evaluate magma emplacement, White Horse Mountains, eastern Nevada, U.S.A.: Tectonophysics, v. 500, p. 98–111, doi:10.1016/j.tecto.2010.05.001.

Marko, W., Barnes, M., Vietti, L., McCulloch, L., Anderson, H., Barnes, C., and Yoshinobu, A., 2005, Xenolith incorporation, distribution, and dissemination in a mid-crustal granodiorite, Vega pluton, central Norway: Eos (Transactions, American Geophysical Union), v. 86, Fall Meeting Supplement, abs. V13E–0596.

Marsh, B.D., 1982, On the mechanisms of igneous diapirism, stoping and zone melting: American Journal of Science, v. 282, p. 808–855, doi:10.2475/ajs.282.6.808.

Mattinson, J.M., 1978, Age, origin, and thermal histories of some plutonic rocks from the Salinian block of California: Contributions to Mineralogy and Petrology, v. 67, p. 233–245, doi:10.1007/BF00381451.

Mattinson, J.M., 2005, Zircon U-Pb chemical abrasion ("CA-TIMS") method: Combined annealing and multi-step partial dissolution analysis for improved precision and accuracy of zircon ages: Chemical Geology, v. 220, p. 47–66, doi:10.1016/j.chemgeo.2005.03.011.

Matzel, J.E.P., Bowring, S.A., and Miller, R.B., 2006, Time scales of pluton construction at differing crustal levels: Examples from the Mount Stuart and Tenpeak intrusions, North Cascades, Washington: Geological Society of America Bulletin, v. 118, p. 1412–1430, doi:10.1130/B25923.1.

McCaffrey, K.J.W., and Petford, N., 1997, Are granitic intrusions scale invariant?: Geological Society of London Journal, v. 154, p. 1–4, doi:10.1144/gsjgs.154.1.0001.

Melezhik, V.A., Roberts, D., Fallick, A.E., Gorokhov, I.M., and Kusnetzov, A.B., 2005, Geochemical preservation potential of high-grade calcite marble versus dolomite marble: Implication for isotope chemostratigraphy: Chemical Geology, v. 216, p. 203–224, doi:10.1016/j.chemgeo.2004.11.020.

Memeti, V., Paterson, S., Matzel, J., Mundil, R., and Okaya, D., 2010, Magmatic lobes as "snapshots" of magma chamber growth and evolution in large, composite batholiths: An example from the Tuolumne intrusion, Sierra Nevada, California: Geological Society of America Bulletin, v. 122, p. 1912–1931, doi:10.1130/B30004.1.

Mezger, K., Raunsley, C.M., Bohlen, S.R., and Hanson, G.N., 1991, U-Pb garnet, sphene, monazite and rutile ages: Implications for the duration of high-grade metamorphism and cooling histories, Adirondack Mountains, New York: Journal of Geology, v. 99, p. 415–428, doi:10.1086/629503.

Mezger, K., Essene, E.J., van der Plujim, B.A., and Halliday, A.N., 1993, U-Pb geochronology of the Grenville orogen of Ontario and New York: constraints on ancient crustal tectonics: Contributions to Mineralogy and Petrology, v. 114, p. 13–26.

Miller, B., and Paterson, S.R., 1999, In defense of magmatic diapirs: Journal of Structural Geology, v. 21, p. 1161–1173, doi:10.1016/S0191-8141(99)00033-4.

Miller, C.F., Furbish, D.J., Walker, B., Claiborne, L.L., Koteas, G.C., Bleick, H.A., and Miller, J.S., 2011, Growth of plutons by incremental emplacement of sheets in crystal-rich host: Evidence from Miocene intrusions of the Colorado River region, Nevada, USA: Tectonophysics, v. 500, p. 65–77, doi:10.1016/j.tecto.2009.07.011.

Myrland, R., 1972, Velfjord. Beskrivelse til det berggrunnsgeologiske gradteigskart I 18 - 1:100,000: Norges Geologiske Undersøkelse Bulletin 274, 30 p.

Nabelek, P.I., Hofmeister, A.M., and Whittington, A.G., 2012, The influence of temperature-dependent thermal diffusivity on the conductive cooling rates of plutons and temperature-time paths I contact aureoles: Earth and Planetary Science Letters, v. 317–318, p. 157–164, doi:10.1016/j.epsl.2011.11.009.

Nordgulen, Ø., 1993, A summary of the petrography and geochemistry of the Bindal Batholith: Norges Geologiske Undersøkelse, v. 92.111, 103 p.

Nordgulen, Ø., and Sundvoll, B., 1992, Strontium isotope composition of the Bindal Batholith, central Norwegian Caledonides: Norges Geologiske Undersøkelse Bulletin, v. 423, p. 19–39.

Nordgulen, Ø., Fjeldheim, T., Ihlen, P.M., Nissen, A.L., and Solli, A., 1992, VEVELSTAD berggrunnskart 1826–3: Norges Geologiske Undersøkelse, scale 1:50,000.

Nordgulen, Ø., Bickford, M., Nissen, A., and Wortman, G., 1993, U-Pb zircon ages from the Bindal Batholith, and the tectonic history of the Helgeland Nappe Complex, Scandinavian Caledonides: Geological Society of London Journal, v. 150, p. 771–783, doi:10.1144/gsjgs.150.4.0771.

Oalmann, J., Barnes, C., and Hetherington, C.J., 2011, Geology of the island of Ylvingen, Nordland, Norway: Evidence for pre-Scandian (~475 Ma) exhumation in the Helgeland Nappe Complex: Norges Geologiske Undersøkelse Bulletin, v. 91, p. 77–99.

Parrish, R.R., Roddick, J.C., Loveridge, W.D., and Sullivan, R.D., 1987, Uranium-lead analytical techniques at the geochronology laboratory, Geological Survey of Canada, *in* Radiogenic age and isotopic studies, Report 1: Geological Survey of Canada Paper 87-2, p. 3–7.

Paterson, S.R., Pignotta, G.S., Farris, D., Memeti, V., Miller, R.B., Vernon, R.H., and Zak, J., 2008, Is stoping a volumetrically significant pluton emplacement process?: Geological Society of America Bulletin, v. 120, p. 1075–1079, doi:10.1130/B26148.1.

Paulatto, M., Annen, C., Henstock, T.J., Kiddle, E., Minshull, T.A., Sparks, R.S.J., and Voight, B., 2012, Magma chamber properties from integrated seismic tomography and thermal modeling at Montserrat: Geochemistry Geophysics Geosystems, v. 13, doi:10.1029/2011GC003892.

Petford, N., 1996, Dykes or diapirs?: Royal Society of Edinburgh Transactions, Earth Sciences, v. 87, p. 105–114, doi:10.1017/S0263593300006520.

Pidgeon, R.T., Bosch, D., and Bruguier, O., 1996, Inherited zircon and titanite U-Pb systems in an Archaean syenite from southwestern Australia: Implications for U-Pb stability of titanite: Earth and Planetary Science Letters, v. 141, p. 187–198, doi:10.1016/0012-821X(96)00068-4.

Pitcher, W.S., 1970, Ghost stratigraphy in intrusive granites: A review, *in* Newall, G., and Rast, N., eds., Mechanisms of igneous intrusion: Liverpool, Gallery Press, p. 123–140.

Richey, J.E., 1927, The structural relations of the Mourne Granites, Northern Ireland: Geological Society of London Quarterly Journal, v. 83, p. 653–688, doi:10.1144/GSL.JGS.1927.083.01-05.27.

Roberts, D., Melezhik, V., and Heldal, T., 2002, Carbonate formations and early NW-directed thrusting in the highest allochthons of the Norwegian Caledonides: Evidence of a Laurentian ancestry: Geological Society of London Journal, v. 159, p. 117–120, doi:10.1144/0016-764901-128.

Rubin, A.M., 1993, Dikes vs. diapirs in visco-elastic rock: Earth and Planetary Science Letters, v. 119, p. 641–659, doi:10.1016/0012-821X(93)90069-L.

Saleeby, J.B., 1990, Progress in tectonic petrogenetic studies in an exposed cross-section of younger (~100 Ma) continental crust, southern Sierra Nevada, California, *in* Salisbury, M.H., and Fountain, D.M., eds. Exposed cross-sections of the continental crust: Netherlands, Kluwer, p. 137–158.

Sandøy, R., 2003, Geological variations in marble deposits. The geometry, internal structure and geochemical variations of the industrial mineral marble deposits in the Velfjord area [Ph.D. thesis]: Trondheim, Norway, Norges Teknisk-Naturvitenskapelige Universitet, 534 p.

Schaltegger, U., Brack, P., Ovtcharova, M., Peytcheva, I., Schoene, B., Stracke, A., Marocchi, M., and Bargossi, G.M., 2009, Zircon and titanite recording 1.5 million years of magma accretion, crystallization and initial cooling in a composite pluton (southern Adamello batholith, northern Italy): Earth and Planetary Science Letters, v. 286, p. 208–218, doi:10.1016/j.epsl.2009.06.028.

Schoene, B., Crowley, J.L., Condon, D.J., Schmitz, M.D., and Bowring, S.A., 2006, Reassessing the uranium decay constants for geochronology using ID-TIMS U–Pb data: Geochimica et Cosmochimica Acta, v. 70, p. 426–445, doi:10.1016/j.gca.2005.09.007.

Schoene, B., Latkoczy, C., Schaltegger, U., and Gunther, D., 2010, A new method integrating high-precision U-Pb geochronology with trace element analysis (U-Pb TIMS-TEA): Geochimica et Cosmochimica Acta, v. 74, p, 7144–7159, doi:10.1016/j.gca.2010.09.016.

Schoene, B., Schaltegger, U., Brack, P., Latkoczy, C., Stracke, A., and Gunther, D., 2012, Rates of magma differentiation and emplacement in a ballooning pluton recorded by U-Pb TIMS-TEA, Adamello batholith, Italy: Earth and Planetary Science Letters, v. 355–356, p. 162–173, doi:10.1016/j.epsl.2012.08.019.

Scott, D.J., and St. Onge, M.R., 1995, Constraints on Pb closure temperature in titanite based on rocks from the Ungava orogen, Canada: Implications for U-Pb geochronology and P-T-t path determinations: Geology, v. 23, p. 1123–1126, doi:10.1130/0091-7613(1995)023<1123:COPCTI>2.3.CO;2.

Shane, P., Storm, S., Schmitt, A.K., and Lindsay, J.M., 2012, Timing and conditions of formation of granitoid clasts erupted in recent pyroclastic deposits from Tarawera volcano (New Zealand): Lithos, v. 140–141, p. 1–10, doi:10.1016/j.lithos.2012.01.012.

Spear, F.S., and Parrish, R., 1996, Petrology and petrologic cooling rates of the Valhalla complex, British Columbia, Canada: Journal of Petrology, v. 37, p. 733–765, doi:10.1093/petrology/37.4.733.

Steiger, R.H., and Jäger, E., 1977, Subcommission on geochronology; convention on the use of decay constants in geo- and cosmochronology: Earth and Planetary Science Letters, v. 36, p. 359–362, doi:10.1016/0012-821X(77)90060-7.

Stern, T.W., Bateman, P.C., Morgan, B.A., Newell, M.F., and Peck, D.L., 1981, Isotopic U-Pb ages of zircon from the granitoids of the central Sierra Nevada, California: U.S. Geological Survey Professional Paper 1185, 17 p.

Thorsnes, T., and Løseth, H., 1991, Tectonostratigraphy in the Velfjord-Tosen region, southwestern part of the Helgeland Nappe Complex: Central Norwegian Caledonides: Norges Geologiske Undersøkelse Bulletin, v. 421, p. 1–18.

Tikoff, B., and Teyssier, C., 1992, Crustal-scale, en echelon P-shear tensional bridges: A possible solution to the batholithic room problem: Geology, v. 20, p. 927–930, doi:10.1130/0091-7613(1992)020<0927:CSEEPS>2.3.CO;2.

Tobisch, O.T., and Paterson, S.R., 1988, Analyses and interpretation of composite foliations in areas of progressive deformation: Journal of Structural Geology, v. 10, p. 745–754, doi:10.1016/0191-8141(88)90081-8.

Tobisch, O.T., Saleeby, J., and Fiske, R.S., 1986, Structural history of continental volcanic arc rocks, eastern Sierra Nevada, California: A case for extensional tectonics: Tectonics, v. 5, p. 65–94, doi:10.1029/TC005i001p00065.

Tobisch, O.T., Saleeby, J., Renne, P.R., McNulty, B., and Tong, W., 1995, Variations in deformation during development of a large volume magmatic arc, Sierra Nevada, California: Geological Society of America Bulletin, v. 107, p. 148–166, doi:10.1130/0016-7606(1995)107<0148:VIDFDD>2.3.CO;2.

Trønnes, R.G., 1994, Marmorforekomester I Midt-Norge: Geolgi isotopgeokjemi of industrimineralpotensaile: Norges Geologiske Undersøkelse Rapport 94.042, 21 p.

Trønnes, R.G., and Sundvoll, B., 1995, Isotopic composition, deposition ages and environments of Central Norwegian Caledonian marbles: Norges Geologiske Undersøkelse Bulletin, v. 427, p. 44–47.

Vernon, R.H., 2004, A practical guide to rock microstructures: Cambridge, Cambridge University Press, 594 p.

Vernon, R.H., Etheridge, M.A., and Wall, V.J., 1988, Shape and microstructure of microgranitoid enclaves: Indicators of magma mingling and flow: Lithos, v. 22, p. 1–11, doi:10.1016/0024-4937(88)90024-2.

Wiebe, R.A., and Collins, W.J., 1998, Depositional features and stratigraphic sections in granitic plutons: Implications for the emplacement and crystallization of granitic magma: Journal of Structural Geology, v. 20, p. 1273–1289, doi:10.1016/S0191-8141(98)00059-5.

Yoshinobu, A.S., and Barnes, C.G., 2008, Is stoping a volumetrically significant pluton emplacement process?: Geological Society of America Bulletin, v. 120, p. 1080–1081, doi:10.1130/B26141.1.

Yoshinobu, A.S., Okaya, D.A., and Paterson, S.R., 1998, Modeling the thermal evolution of fault-controlled magma emplacement models: Implications for the solidification of granitoid plutons: Journal of Structural Geology, v. 20, p. 1205–1218, doi:10.1016/S0191-8141(98)00064-9.

Yoshinobu, A.S., Barnes, C.G., Nordgulen, Ø., Prestvik, T., Fanning, M., and Pedersen, R.B., 2002, Ordovician magmatism, deformation, and exhumation in the Caledonides of central Norway: An orphan of the Taconic orogeny?: Geology, v. 30, p. 883–886, doi:10.1130/0091-7613(2002)030<0883:OMDAEI>2.0.CO;2.

Yoshinobu, A.S., Wolak, J.M., Paterson, S.R., Pignotta, G.S., and Anderson, H.S., 2009, Determining relative magma and host rock xenolith rheology during magmatic fabric formation in plutons: Examples from the middle and upper crust: Geosphere, v. 5, p. 270–285, doi:10.1130/GES00191.1.